

REVIEW SUMMARY

APPLIED PHYSICS

2D materials and van der Waals heterostructures

K. S. Novoselov,* A. Mishchenko, A. Carvalho, A. H. Castro Neto*

BACKGROUND: Materials by design is an appealing idea that is very hard to realize in practice. Combining the best of different ingredients in one ultimate material is a task for which we currently have no general solution. However, we do have some successful examples to draw upon: Composite materials and III-V heterostructures have revolutionized many aspects of our lives. Still, we need a general strategy to solve the problem of mixing and matching crystals with different properties, creating combinations with predetermined attributes and functionalities.

ADVANCES: Two-dimensional (2D) materials offer a platform that allows creation of heterostructures with a variety of properties. One-atom-thick crystals now comprise a large family of these materials, collectively covering a very

broad range of properties. The first material to be included was graphene, a zero-overlap semimetal. The family of 2D crystals has grown to include metals (e.g., NbSe₂), semiconductors (e.g., MoS₂), and insulators [e.g., hexagonal boron nitride (hBN)]. Many of these materials are stable at ambient conditions, and we have come up with strategies for handling those that are not. Surprisingly, the properties of such 2D materials are often very different from those of their 3D counterparts. Furthermore, even the study of familiar phenomena (like superconductivity or ferromagnetism) in the 2D case, where there is no long-range order, raises many thought-provoking questions.

A plethora of opportunities appear when we start to combine several 2D crystals in one vertical stack. Held together by van der Waals forces (the same forces that hold layered ma-

terials together), such heterostructures allow a far greater number of combinations than any traditional growth method. As the family of 2D crystals is expanding day by day, so too is the complexity of the heterostructures that could be created with atomic precision.

When stacking different crystals together, the synergetic effects become very important. In the first-order approximation, charge

redistribution might occur between the neighboring (and even more distant) crystals in the stack. Neighboring crystals can also induce structural changes in each other.

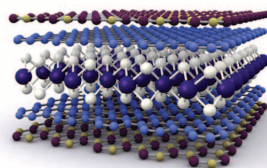
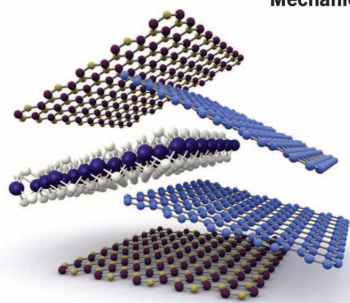
Furthermore, such changes can be controlled by adjusting the relative orientation between the individual elements.

Such heterostructures have already led to the observation of numerous exciting physical phenomena. Thus, spectrum reconstruction in graphene interacting with hBN allowed several groups to study the Hofstadter butterfly effect and topological currents in such a system. The possibility of positioning crystals in very close (but controlled) proximity to one another allows for the study of tunneling and drag effects. The use of semiconducting monolayers leads to the creation of optically active heterostructures.

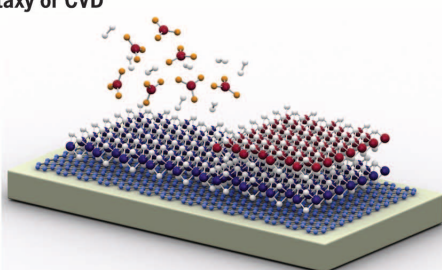
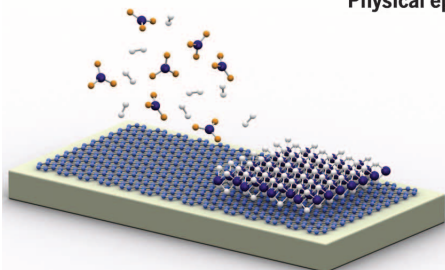
The extended range of functionalities of such heterostructures yields a range of possible applications. Now the highest-mobility graphene transistors are achieved by encapsulating graphene with hBN. Photovoltaic and light-emitting devices have been demonstrated by combining optically active semiconducting layers and graphene as transparent electrodes.

OUTLOOK: Currently, most 2D heterostructures are composed by direct stacking of individual monolayer flakes of different materials. Although this method allows ultimate flexibility, it is slow and cumbersome. Thus, techniques involving transfer of large-area crystals grown by chemical vapor deposition (CVD), direct growth of heterostructures by CVD or physical epitaxy, or one-step growth in solution are being developed. Currently, we are at the same level as we were with graphene 10 years ago: plenty of interesting science and unclear prospects for mass production. Given the fast progress of graphene technology over the past few years, we can expect similar advances in the production of the heterostructures, making the science and applications more achievable. ■

Mechanically-assembled stacks



Physical epitaxy or CVD



Production of van der Waals heterostructures. Owing to a large number of 2D crystals available today, many functional van der Waals heterostructures can be created. What started with mechanically assembled stacks (**top**) has now evolved to large-scale growth by CVD or physical epitaxy (**bottom**).

The list of author affiliations is available in the full article online.

*Corresponding author. Email: kostya@manchester.ac.uk (K.S.N.); phycast@nus.edu.sg (A.H.C.N.)

Cite this article as K. S. Novoselov et al., *Science* 353, aac9439 (2016). DOI: 10.1126/science.aac9439

REVIEW

APPLIED PHYSICS

2D materials and van der Waals heterostructures

K. S. Novoselov,^{1,2*} A. Mishchenko,^{1,2} A. Carvalho,³ A. H. Castro Neto^{3*}

The physics of two-dimensional (2D) materials and heterostructures based on such crystals has been developing extremely fast. With these new materials, truly 2D physics has begun to appear (for instance, the absence of long-range order, 2D excitons, commensurate-incommensurate transition, etc.). Novel heterostructure devices—such as tunneling transistors, resonant tunneling diodes, and light-emitting diodes—are also starting to emerge. Composed from individual 2D crystals, such devices use the properties of those materials to create functionalities that are not accessible in other heterostructures. Here we review the properties of novel 2D crystals and examine how their properties are used in new heterostructure devices.

The family of two-dimensional (2D) materials (1) has grown appreciably since the first isolation of graphene (2). The emergence of each new material brings excitement and puzzles, as the properties of these materials are usually very different from those of their 3D counterparts. Furthermore, 2D materials offer great flexibility in terms of tuning their electronic properties. Thus, band-gap engineering can be carried out by changing the number of layers in a given material (3, 4). Even more interesting is the specific 2D physics observed in such materials [for instance, Kosterlitz-Thouless (KT) behavior, characterized by the emergence of topological order, resulting from the pairing of vortices and antivortices below a critical temperature]. Crystals with transition metals in their chemical composition are particularly prone to many-body instabilities such as superconductivity, charge density waves (CDWs), and spin density waves (SDWs). Such effects can also be induced by proximity if such crystals are sandwiched with other 2D materials.

Not only do heterostructures of 2D materials offer a way to study these phenomena, they also present unprecedented possibilities of combining them for technological use. Such stacks are very different from the traditional 3D semiconductor heterostructures, as each layer acts simultaneously as the bulk material and the interface, reducing the amount of charge displacement within each layer. Still, the charge transfers between the layers can be very large, inducing large electric fields and offering interesting possibilities in band-structure engineering.

Among the tools for band-structure engineering in van der Waals heterostructures are the relative alignment between the neighboring crystals, surface reconstruction, charge transfer, and proximity effects (when one material can borrow the property of another by contact via quantum tunneling or by Coulomb interactions). Thus, a moiré structure for graphene on hexagonal boron nitride (hBN) leads to the formation of secondary Dirac points (5–9), commensurate-incommensurate transition in the same system leads to surface reconstruction (10) and gap opening in the electron spectrum (8), and spin-orbit interaction can be enhanced in graphene by neighboring transition metal dichalcogenides (TMDCs) (11, 12).

Here we provide a review of 2D materials, analyzing the physics that can be observed in such crystals. We discuss how these properties are put to use in new heterostructure devices.

Transition metal dichalcogenides

Transition metal dichalcogenides, with the formula MX_2 (where M is a transition metal and X is a chalcogen), offer a broad range of electronic properties, from insulating or semiconducting (e.g., Ti, Hf, Zr, Mo, and W dichalcogenides) to metallic or semimetallic (V, Nb, and Ta dichalcogenides). The different electronic behavior arises from the progressive filling of the nonbonding d bands by the transition metal electrons. The evolution of the electronic density of states (DOS) is shown in Fig. 1 [adapted from (13–17)] for the most stable phase of each of the dichalcogenides.

All TMDCs have a hexagonal structure, with each monolayer comprising three stacked layers (X-M-X). The two most common polytypes of the monolayers are trigonal prismatic (e.g., MoS_2 and WS_2) and octahedral (e.g., TiS_2); these terms refer to the coordination of the transition metal atom. Inversion symmetry is broken in the former, giving rise to piezoelectricity and having important consequences for the electronic structure. In addition, many of the tellurides, TeS_2 , ReS_2 , and

other dichalcogenides adopt lower-symmetry structures in which the metal atom is displaced away from the center of the coordination unit.

Metallic TMDCs

As shown in Fig. 1, the DOS of metallic TMDCs has two main properties: (i) The Fermi level of the undoped material is always crossing a band with d-orbital character, implying that the electrons move mostly in the metal layers, and (ii) the DOS at the Fermi level is usually quite high, which hints at a common explanation for the phase transitions observed in these materials (18).

The interest in these materials comes from the existence of CDWs and superconductivity in their phase diagrams (19). Whereas the CDW phase has clear insulating tendency (opening a gap and suppressing the DOS at the Fermi level), the superconducting phase needs finite DOS to exist, resulting in a direct competition between the two many-body states. This competition leads to a complex phase diagram with the presence of inhomogeneous electronic and structural patterns, which have been observed in electron microscopy and neutron scattering in the 3D parent compound. Measurements of specific heat and magnetic susceptibility in 3D samples have shown partial gapping of the Fermi surface. In some cases (e.g., TaS_2), the CDW transition leads to the decoupling of the unit cells along the axis perpendicular to the planes, with an enormous increase in transverse resistivity.

These unusual properties of metal TMDCs have been the subject of intense theoretical debate, but no consensus has been reached. The mechanism for the CDW transition does not fit standard weak-coupling mean field theories such as Fermi surface nesting or transitions induced by van Hove singularities. Many angle-resolved photoemission experiments have been performed in 3D samples with contradictory results (20). The existence of several Fermi surface sheets and the partial gapping of the Fermi surface make the theoretical interpretation of the experimental data quite difficult. Furthermore, the coexistence of CDWs and superconductivity (clearly seen in local probes) (21) indicates that many-body effects play a very important role in these materials.

Critical information can be obtained from transport data in these materials, when transport measurements are performed in conjunction with the application of electric and magnetic fields. External electric field changes the Fermi energy and the carrier concentration in the 2D material, without the need for chemical doping (which was the case in 3D materials and which introduces appreciable disorder).

In a recent experiment on 1T-TiSe_2 , a 2D film was encapsulated by hBN and subjected to transverse electric and magnetic fields (22). By applying an external electric field to change the carrier density, it was possible to tune the CDW transition temperature from 170 to 40 K and, concomitantly, the superconducting transition temperature from 0 to 3 K. Controlling the transition temperatures using an electric field allows the critical exponents for the phase transition to be determined

¹School of Physics and Astronomy, University of Manchester, Oxford Road, Manchester M13 9PL, UK. ²National Graphene Institute, University of Manchester, Manchester M13 9PL, UK. ³Centre for Advanced 2D Materials and Graphene Research Centre, National University of Singapore, 2 Science Drive 3, Singapore 117542.

*Corresponding author. Email: kostya@manchester.ac.uk (K.S.N.); phycast@nus.edu.sg (A.H.C.N.)

with high accuracy. Moreover, applying an external transverse magnetic field at the same time reveals novel physical phenomena associated with periodic motion of the Cooper pairs in the superconducting phase. Such behavior seems to be tied up with the formation of discommensurations between different CDW domains—namely, the electronic system broke down in perfectly ordered superconducting and CDW domains.

Phase transitions in 2D materials

Electrons in a solid are characterized by several quantum numbers that include charge and spin. Due to electron-electron or electron-ion interactions, electrons can organize themselves in phases characterized by an order parameter that is associated with these degrees of freedom. In a CDW state, as in the case of TMDCs, the order parameter is the local electron density $\rho(\mathbf{r})$, where \mathbf{r} is the position vector, which orders with a well-defined periodicity. This periodicity implies that the Fourier transform of the density, $\rho(\mathbf{Q})$, where \mathbf{Q} is the so-called ordering wave vector of the CDW, acquires a finite expectation value. For a CDW, the expectation value of $\rho(\mathbf{Q})$ is the order parameter, which is zero in the disordered (or normal) phase and finite in the ordered phase. The transition between these phases can be driven by external forces such as electric, mechanical, and thermal.

Two-dimensional systems play a particular role in the physics of phase transitions. For a system with a continuous order parameter, it is not possible to have true long-range order in less than three dimensions at any finite temperature T , implying that even minute thermal fluctuations can destroy order (23). In two dimensions, long-range order is possible only at strictly zero temperature. At $T = 0$, it is also possible for a system to be disordered if one varies an external parameter such as pressure or electric field, E (Fig. 2). The point at which a system becomes ordered at $T = 0$ is called the quantum critical point, and the transitions are called quantum phase transitions. In this case, it is not thermal motion that drives the system from order to disorder but quantum fluctuations. In this type of transition, the scale at which order is created is characterized by a correlation length ξ , which diverges at the phase transition as

$$\xi(E) \sim 1/|E - E_c|^\nu$$

where E_c is the critical field and ν is the critical exponent. Fluctuations of the order parameter at different points in space decay exponentially with ξ . Variations in length scales lead to fluctuations in energy scales as well. In a second-order phase transition, the characteristic energy scale, Δ , associated with the particular order (that is, the energy gap in the system) vanishes at the phase transition with another dynamical exponent, z , as

$$\Delta(E) \sim 1/\xi^z \sim |E - E_c|^{z\nu}$$

The simplest theory for understanding the effect of critical fluctuations close to a phase transition assumes that the order parameter

(SDW, CDW, etc.) couples locally with the relevant degree of freedom (spin, charge, etc.). The resistivity is then given by the standard de Gennes–Friedel formula, in which the electron mean free path scales with the differential scattering cross section of the order parameter fluctuations.

In a classical phase transition, the behavior is driven by thermal fluctuations. The resistivity has

the same kind of singularity as internal energy, implying that the critical behavior of the derivative of the resistivity is the same as the specific heat at the phase transition. This indicates that in a classical phase transition the critical behavior is marked by an inflection point in the resistivity at T_c .

Even though, for a 2D system, long-range order is not possible at any finite temperature, the

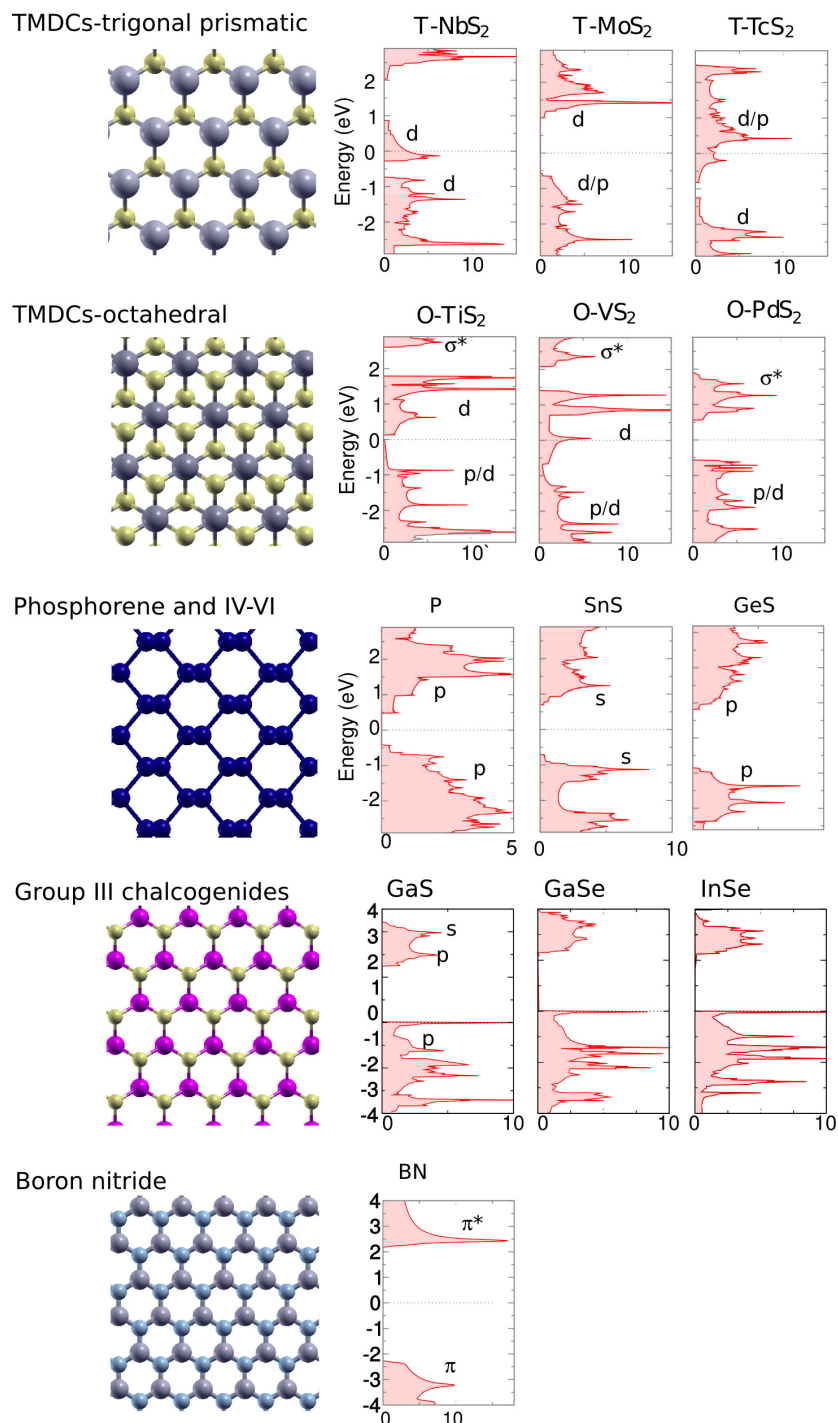


Fig. 1. Electronic properties of different classes of 2D materials. The Fermi level is set to the zero of the energy scale. The DOS is given in states per electron volt per cell.

system can undergo a transition to quasi-long-range order (KT transition) with the presence of vortex-antivortex pairs (24). In this case, the order parameter correlation length obeys the exponential dependence with temperature T

$$\xi(T) \sim a \exp(b/|T - T_{KT}|^{1/2}),$$

where a and b are constants and $T_{KT}(E)$ is the KT transition temperature, which is a function of the external tuning parameter E . The resistivity scales with some power of the inverse correlation length and hence is supposed to have an exponential dependence with temperature.

Semiconducting group-VIB dichalcogenides

Because of the charge confinement and reduced dielectric screening, the optical properties of semiconducting 2D materials are dominated by excitonic effects. The optical spectra of MoS₂, one of the most studied TMDCs, is characterized by three main transitions, named the A, B, and C peaks. The A exciton is the lowest energy corresponding to the fundamental optical gap of the material. The corresponding exciton binding energy is ~ 1 eV, according to theory. The B exciton also corresponds to a transition at the K point but for opposite spin. The C peak is of a different nature, as it has contributions from excitons from a large, annular-shaped region of the k -space with nearly identical transition energies. In nearly neutral monolayer samples, other quasiparticles have been observed, including positively and negatively charged excitons (i.e., trions) and biexcitons (25–27). The large trion binding energies (20 to 30 meV) have no parallel in traditional semiconductors and allow for these quasiparticles to be observed even at room temperature.

The series of Rydberg exciton states above the 1-s (A) exciton of WS₂ reveals an exciton series that deviates considerably from the hydrogen model (28, 29). Not only do the 1s, 2s, 3s, ... ns states have a closer spacing for small n , reflecting a weaker screening at short range ($\sim \log r$, where r is the electron-hole separation) (28), they also have an entirely different dependence on the angular momentum. Ab initio GW calculations show that the states in the same shell but with higher angular momentum are at lower energy levels—that is, 3d, 3p, and 3s are in order of increasing energy.

From the technological point of view, however, the most relevant transitions are those close to the fundamental gap at $K(K')$ points of the Brillouin zone, which can be used for manipulating quantum information stored as spin and momentum (valley index) of individual electrons, holes, or excitons. The selection rule for optical transitions is valley-dependent, with the $K(K')$ valley coupling exclusively to right (left) circularly polarized light. Thus, the valley index, or pseudospin, can be controlled coherently by using polarized light. Because the two valleys have non-zero and symmetrical Berry curvature, in the pres-

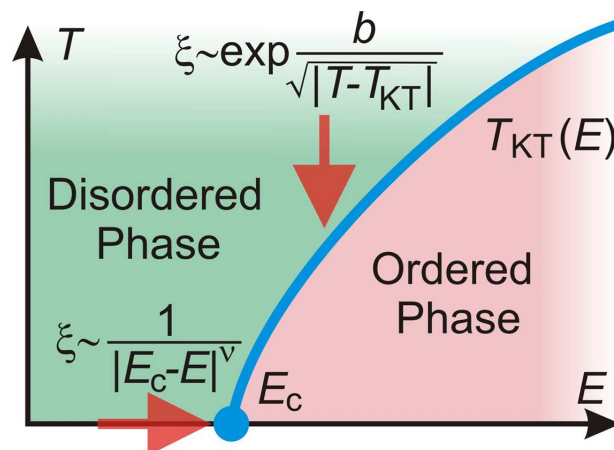


Fig. 2. Phase diagram for a 2D material with a quantum phase transition.

ence of in-plane electric field they give rise to Hall currents with sign depending on the valley index, an effect known as the valley Hall effect. The orbital magnetic moment is also valley-dependent, which allows for coupling with magnetic fields (30–36).

Quantum dots of TMDCs inherit the valley properties of the monolayer and therefore are appealing for valleytronics due to the possibility of controlling spin and valley states of single confined electrons or holes—for example, via interaction with propagating single photons. Quantum dots can be created by growing finite islands on a monolayer substrate or by applying confinement potentials using patterned electrodes.

Phosphorene and group-IV monochalcogenides

Phosphorene, a monolayer of black phosphorus, is a monoelemental 2D material. Monolayer, few-layer, and bulk black phosphorus are all semiconducting materials, with a direct or nearly direct band gap (4). Additionally, phosphorene has a very high mobility that can reach 1000 cm²/V-s for devices of ~ 10 -nm thickness at room temperature (37). This exceeds the carrier mobility of TMDCs. According to theoretical predictions, the phonon-limited hole mobilities can reach 10,000 to 26,000 cm²/V-s for the monolayer (zigzag direction) (38).

Both the optical and transport properties of phosphorene are highly anisotropic, as a consequence of this material's orthorhombic, wavelike structure. Optical selection rules dictate that the absorption threshold is lower for linear polarized light along the armchair direction than along the perpendicular direction. Optical conductivity and Raman spectra are also anisotropic, providing a fast way to determine phosphorene's lattice orientation. In addition to its optical and electronic properties, fundamental research in phosphorene has unraveled a growing number of physical phenomena, including superconductivity, high thermoelectric figure of merit (39), birefringence, and colossal ultraviolet (UV) absorption.

The group-IV monochalcogenides SnS, GeS, SnSe, and GeSe are isoelectronic with phosphor-

ene and share its orthorhombic structure, but the two-atom types break the inversion symmetry of the monolayer. As a consequence, they feature spin-orbit splitting (19 to 86 meV) (40) and piezoelectricity with large coupling between deformation and polarization change in plane (with piezoelectric coefficients e_{33} ranging from 7×10^{-10} to 23×10^{-10} C/m, largely exceeding those of MoS₂ and hBN) (41).

SnS, SnSe, and GeSe are semiconductors, with gap energies covering part of the infrared and visible range for different numbers of layers (40). Even though the indirect band gap (in most cases) makes these materials less attractive for optical applications, the existence of two pairs of twofold degenerate valence and conduction band valleys, each placed on one principal axis of the Brillouin zone, makes them suitable for valleytronics applications.

In this case, the symmetry is orthorhombic and, thus, the valley manipulation processes are different from those for TMDCs. Valley pairs can be selected using linear rather than circularly polarized light. Furthermore, there is no valley Hall effect, so the transverse valley current under an electric field is a second-order effect. Group-IV monochalcogenides are more stable against oxidation than phosphorene, can be grown by chemical vapor deposition (CVD), and have been recently exfoliated down to their bilayers.

Gallium and indium monochalcogenides

GaX and InX (where X is a chalcogen, like S, Se, or Te) are additional members of the family of hexagonal 2D materials. In this case, each layer can be viewed as a double layer of metal $M = \text{Ga}$, intercalated between two layers of chalcogen (X-M-M-X). The band structure of monolayers of such materials is rather unusual, having a “Mexican hat” dispersion at the top of the valence band, leading to a high DOS (42, 43) (bulk materials are most probably direct band-gap semiconductors). Thus, these materials have high and fast photoresponsibility (44, 45) and large second-harmonic generation and have attracted attention mostly due to their optical properties. If the Fermi level is close to this singularity in p-doped materials, a ferromagnetic instability arises (46).

Hexagonal boron nitride

Layers of hBN consist of hexagonal rings of alternating B and N atoms, with strong covalent sp² bonds and a lattice constant nearly identical to that of graphite. hBN is very resistant both to mechanical manipulation and chemical interactions and also has a large band gap in the UV range. For these reasons, hBN is a material of choice as an encapsulating layer or substrate for 2D stacked devices, providing an atomically smooth surface free of dangling bonds and charge traps. hBN substrates leave the band structure of graphene near the Dirac point virtually unperturbed (if crystallographic orientations of the two crystals are misaligned) and dramatically improve the mobility of graphene devices (47, 48).

Oxide layers and other insulators

Many oxides have layered structures and can therefore be seen as a source for new 2D materials. These include lead oxide and lead salts [PbO, Pb₂O(SO₄), Na₂PbO₂, etc.], phosphorus oxides and phosphates, molybdenum and vanadium oxides, and other transition metal oxides. In these materials, the layers are often connected by weak covalent bonds, oxygen bridges, or intercalating elements and are normally nonstoichiometric (due to the presence of oxygen vacancies). Further, layered oxides are normally polycrystalline, and mechanical exfoliation methods are usually limited to those available in higher-quality crystals. For the chemical means of production of such monolayers, intercalation with bulky guest species (such as tetrabutylammonium ions) has been used. Some of these layered oxides have been studied due to their importance as battery cathode materials (e.g., MoO₃, V₂O₅, and other Mo and V oxides), superconductors (e.g., copper and cobalt layered oxides) (49, 50), passivating layers (phosphorus oxide) (51, 52), and other areas of technological interest. Layered oxides allow for alloying, combination of different layers, and intercalation of ions and molecules; the possibilities of materials design are immense.

Among the most studied 2D insulators are hybrid perovskites, which are noteworthy for their high optical absorption coefficient within the solar spectrum and strong luminescence. Thin-film perovskite-based solar cells have emerged with a 20% power conversion efficiency, a notable value for a new technology (53). A hybrid perovskite is formed by layers of a metal halide intercalated with layers of organic chains. The high solar cell efficiency is thought to be greatly attributable to the confinement of excitons to the layers. Few-layer hybrid perovskites have been isolated by mechanical exfoliation and found to be stable in air in a time scale of minutes.

Novel van der Waals heterostructures

Two-dimensional crystals can be assembled into heterostructures (54), where the monolayers are held together by van der Waals forces. Considering that a large number of 2D crystals is currently available, it should be possible to create a substantial variety of heterostructures. However, the assembly technique currently in use (micro-mechanical stacking), allows only certain combinations of the interfaces. At the same time, an alternative technique, which potentially allows mass production of such structures (i.e., sequential growth of monolayers) comes with its own limitations and is presently in its infancy. Nevertheless, a large variety of novel experiments and prototypes have already been carried out with van der Waals heterostructures, which indicates that these materials are versatile and practical tools for future experiments and applications.

Assembly techniques

Currently, the most versatile technique for heterostructure assembly is direct mechanical assembly. This technique flourished starting in 2010 with Dean *et al.*'s work, which demonstrated the

very high performance of graphene devices placed on an hBN substrate (47).

The technique used in the early works is based on preparing a flake of 2D crystal (Fig. 3, A to F) on a sacrificial membrane, aligning and placing it on another flake, and then removing the membrane. The process is then repeated to deposit

further layers. Although the crystals are exposed to sacrificial membrane and solvents, which can contaminate the interface, annealing allows one to remove the contaminants and achieve very high interface quality (55), reaching high mobility ($\sim 10^6$ cm²/V·s) in graphene devices prepared this way.

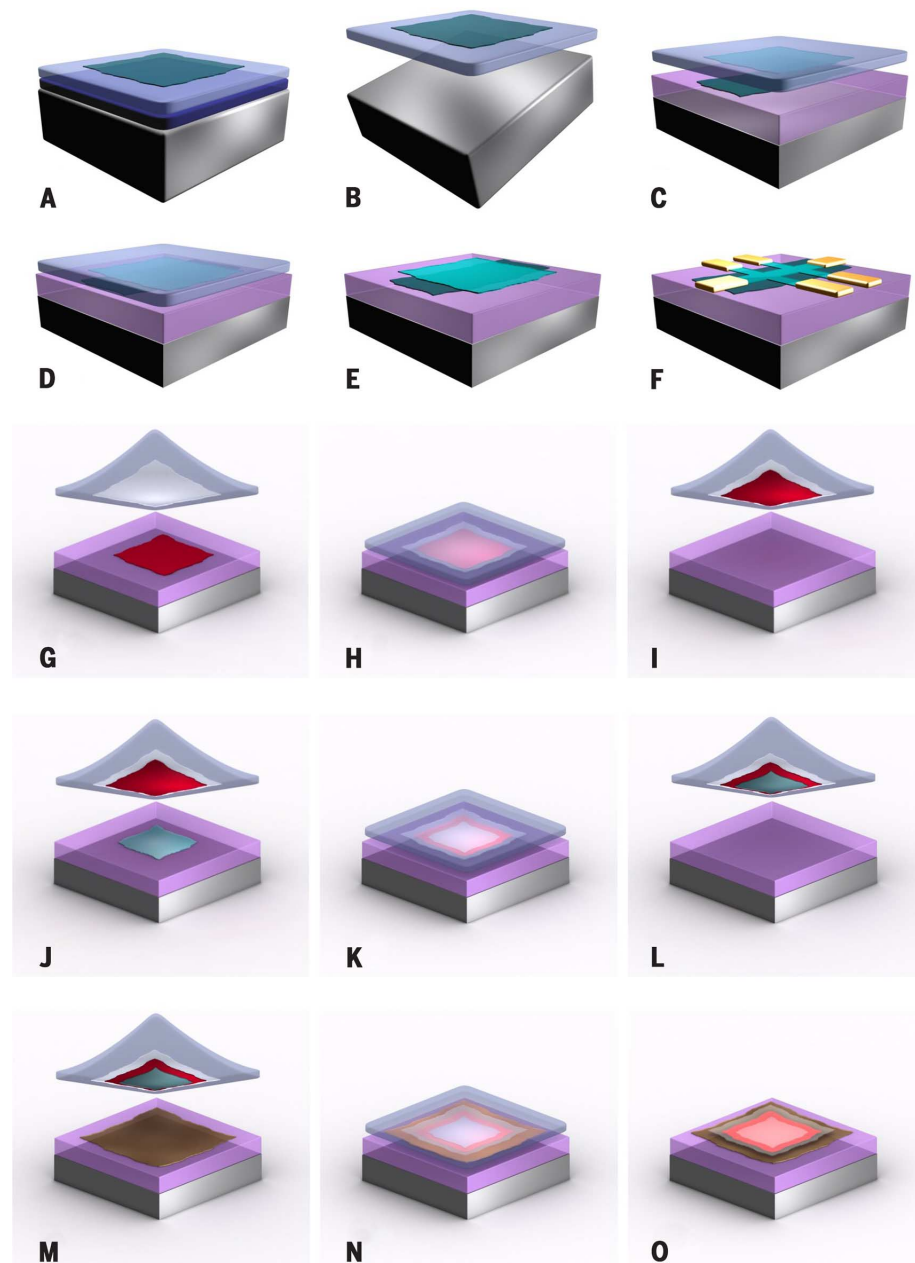


Fig. 3. Wet-transfer and pick-and-lift techniques for assembly of van der Waals heterostructures.

(A to F) Wet-transfer technique. A 2D crystal prepared on a double sacrificial layer (A) is lifted on one layer by dissolving another (B). The crystal is then aligned (C) and placed (D) on top of another 2D material. Upon the removal of the membrane (E), a set of contacts and mesa can be formed (F). This process could be repeated to add more layers on top. (G to O) Pick-and-lift technique. A 2D crystal on a membrane [see (B)] is aligned (G) and then placed atop another 2D crystal (H). Depending on the relative size of the two crystals, it is possible to lift both flakes on the same membrane (I). By repeating the process, it is possible to then lift additional crystals [(J) to (L)]. Finally, the whole stack is placed on the crystal, which will serve as the substrate [(M) and (N)], and the membrane is dissolved, exposing the entire stack (O).

A substantially cleaner method (dubbed the “pick-and-lift” method) is based on strong van der Waals interactions that exist between the crystals. When the membrane with a 2D crystal on it is brought into contact with another 2D crystal, it is not dissolved but rather is lifted up (Fig. 3, G to O); then there is a chance that the second crystal will stick to the first and will be lifted together with it. The process can be repeated several times. This technique results in clean interfaces over large areas and yet higher electron mobility (56). Further advances could be achieved by transferring the whole process into a glovebox with a controllable atmosphere.

1D contacts

The later method (Fig. 3, G to O) has one particular disadvantage: Having a completely assembled stack would prohibit one to make contacts to the inner layer. Luckily, it has been demonstrated that one can achieve various profiles of the edges of such a stack by reactive plasma etching. Thus, it is possible to etch the edge of the stack in such a way that the desired layer becomes exposed and can be contacted by metal evaporation (56) (Fig. 4A). The contact resistance for graphene can be as low as 35 ohm- μm .

Self-cleansing mechanism

The transmission electron microscopy (TEM) studies (55) demonstrate that interfaces can be atomically flat and free of any contamination [Fig. 4, B to D; adopted from (55)]. The reason for such behavior is the so-called “self-cleansing” mechanism (57). If the affinity between the two 2D crystals is larger than the affinity between the crystals and the contaminants, then the energetically favorable situation is when the two crystals have the largest possible common interface. To achieve this condition, the contaminants are pushed away. This explains the observation of bubbles under transferred 2D crystals: Those are the pockets of contamination pushed from the rest of the interface [Fig. 4, E to J; adapted from (57)]. This self-cleansing mechanism works only on certain pairs of crystals (Fig. 4, E to G).

Surface reconstruction

Potentially, the van der Waals interaction between two 2D crystals might lead to surface reconstruction. The most suitable candidates for the observation of such effects are crystals with similar lattice constants, such as graphene on hBN. The lattice constant of hBN is only 1.8% larger than that of graphene, which leads to the formation of a moiré pattern (5).

It has been demonstrated that the most favorable configuration for graphene on hBN is when boron atoms lay on top of one of the sublattices in graphene and nitrogen is situated at the center of the hexagon (58). Then, by stretching itself to match the interatomic spacing of hBN, graphene tries to increase the area where the favorable configuration is achieved. Owing to the high Young modulus of graphene, such perfect stacking cannot be achieved across the whole interface (unless the hBN can contract, as the loss in

elastic energy would not be compensated by the gain in the van der Waals interaction). Thus, such stretching of graphene can only be local, and the stretched regions would be separated by areas where the graphene lattice is not commensurate with hBN (Fig. 4, K and L).

This effect has been observed for graphene on hBN when the crystallographic orientations of the two crystals are practically aligned (10). In this case, the large regions of the moiré pattern where the two crystals are commensurate are separated by areas where the graphene lattice is relaxed. This effect disappears when the graphene is misoriented with respect to hBN. Such commensurate-incommensurate transition happens at a critical angle, which is given by the crystal mismatch (10).

Stacks of several other 2D crystals—including MoS₂ and MoSe₂ (59), MoS₂ and WS₂ (60), fluoro-

graphene and MoS₂ (61), and many others—have been investigated for electronic properties (62) and possible surface reconstruction. Thus, layer-breathing phonon modes have been observed by means of Raman spectroscopy for MoSe₂/MoS₂ heterobilayers (63). However, because the lattice-constant mismatch for those pairs is usually above 2%, the surface reconstruction would be hard to observe. It has been experimentally detected for silicene on MoS₂, where vertical buckling of silicene allows perfect stacking between the two crystals (64).

Spectrum reconstruction for graphene on hBN

Moiré patterns in graphene on hBN provide periodic scattering potential for electrons. This leads to the reconstruction of the electronic spectrum in graphene at the wave vectors determined by the

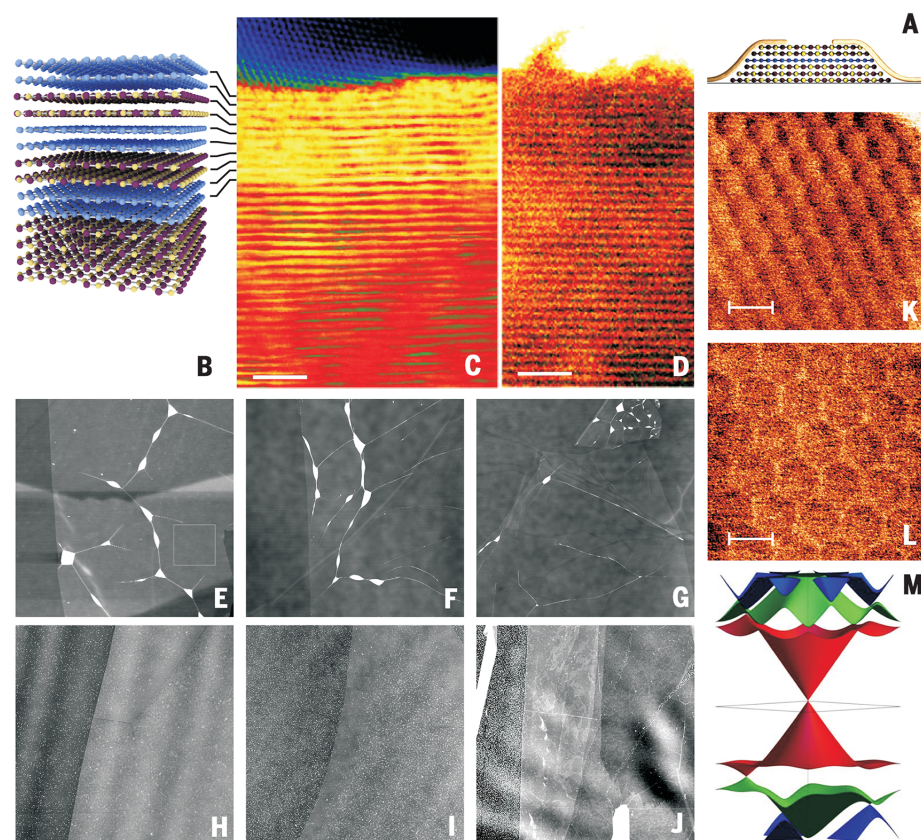


Fig. 4. Morphology of the van der Waals heterostructures. (A) 1D contacts to van der Waals heterostructures. Etching mesa in van der Waals heterostructures exposes the edges of the crystals inside the stack, which allows formation of 1D contacts. Here, carbon atoms are represented by blue spheres, boron is shown in yellow, and nitrogen is in purple. (B to D) TEM cross section of a graphene/hBN heterostructure. (B and C) Scanning TEM image (C) of the structure schematically presented in (B). In (B), atom coloring is the same as in (A). (D) High-angle annular dark-field image of the same stack. Scale bars in (C) and (D), 2 nm. (E to J) Atomic force microscopy (AFM) images of graphene transferred on other 2D crystals. A self-cleansing mechanism pushes contamination (hydrocarbons) away from graphene on hBN (E), MoS₂ (F), and WS₂ (G) interfaces, forcing the contamination to gather in bubbles. Instead, on the substrates with poor adhesion to graphene—such as mica (H), BSCCO (I), and V₂O₅ (J)—contamination is spread uniformly across the whole interface. Images in (E) to (J) are 15 μm by 15 μm , with a z scale of 4 nm. (K and L) Local Young modulus for graphene on hBN for misorientation angles of 3° (K) and 0° (L). Note the sharp domain walls in (L). Scale bars, 14 nm. (M) Reconstructed electronic energy spectrum for graphene aligned on hBN.

periodicity of the moiré structure, as has been observed in scanning tunneling microscopy (5) and, later, in transport (6–8) and capacitance (9) measurements. Secondary Dirac points appear in the electronic spectrum, in both the valence and conduction bands [Fig. 4M; adapted from (65)]. The energy range where the spectrum is reconstructed is given by the strength of the van der Waals interaction between graphene and hBN and is estimated to be on the order of 50 meV. Furthermore, the surface reconstruction leads to the strong asymmetry between the sublattices in graphene, which opens a gap in the graphene spectrum.

Capacitively coupled van der Waals heterostructures

Conceptually, the simplest devices based on van der Waals heterostructures are those for capacitance measurements. hBN is an ideal insulator that can sustain large electric fields (0.5 V per layer and above), allowing the preparation of capacitors with a very thin dielectric. The use of a thin dielectric ensures a large contribution of the quantum capacitance, which is directly proportional to the DOS in the electrode, making capacitance measurements a viable tool to study both single-particle and interaction phenomena in 2D materials. A number of systems have been investigated so far, including quantum capacitance in graphene (66), various sandwiches of graphene with TMDCs (57), and black phosphorus (67).

Capacitive coupling between two graphene layers through a thin layer of hBN can also lead to a number of noteworthy phenomena. This method allows for very-high-quality Coulomb drag devices, where two graphene layers, separated galvanically, interact through Coulomb forces between the charge carriers in the two layers (68). Because it is an atomically flat crystal with a very large gap in the electronic spectrum, hBN allows very thin barriers (on the order of a few nanometers) before any tunneling kicks in, bringing the two graphene layers closer than the characteristic distance between electrons in each of the layers (10 nm for a characteristic density of 10^{12} cm^{-2}). This opens the new regime of effective zero-layer separation in Coulomb drag experiments.

Tunneling devices

Graphene can be combined with semiconductor and insulating 2D crystals to create a tunnel junction (69). The use of hBN as a tunneling barrier is particularly attractive due to its large band gap (~6 eV), low number of impurity states within the barrier, and high breakdown field. Because the position of the Fermi energy and the DOS in graphene can be varied by external gate, the same applies for the tunneling current, which allows such structures to be used as field-effect tunneling transistors (FETTs) (70).

The architecture of FETTs enables tunneling spectroscopy to probe DOS in graphene, as well as to observe impurity- and phonon-assisted tunneling (71). Elastic tunneling through impurities gives peaks in dI/dV_b (I , current; V_b , bias voltage); peak positions depend on both bias and gate

voltages (Fig. 5C). On the other hand, inelastic phonon-assisted tunneling is characterized by a set of plateaus in dI/dV_b , independent of gate voltage (71) [more pronounced in d^2I/dV_b^2 (Fig. 5B)]. When the bias voltage is large enough to emit a phonon ($eV_b = \hbar\omega_{\text{ph}}$, where e is the electron charge, \hbar is Planck's constant h divided by 2π , and ω_{ph} is the frequency of the emitted phonon), an additional channel opens for electron tunneling, which increases transmission probability and, hence, tunnel conductance. Tunneling through impurities and with the phonon emission is especially visible if the crystallographic lattices of the two graphene electrodes are strongly misoriented with respect to each other, which prohibits direct electron tunneling because it is impossible to fulfill the momentum conservation requirements.

If the crystallographic lattices of the two graphene electrodes are aligned, momentum conservation for tunneling electrons can be achieved without impurity or phonon scattering. Rotational misalignment of the two graphene crystals corresponds to a relative rotation of the two graphene Brillouin zones in the reciprocal space. If the misalignment is small enough (<2°), then the momentum difference between the electronic states in the top and bottom graphene layers can be compensated electrostatically by applying bias and gate voltages (72), leading to the resonant tunneling and observation of the negative differential resistance (72) (Fig. 5D). A sharp negative differential resistance feature allows one to build a tunable radio-frequency oscillator with the potential to reach subterahertz frequencies.

The highest on-off ratio for FETTs can be achieved if the changes in the Fermi energy in graphene are comparable with the gap in the tunneling barrier—the situation achieved if hBN is replaced with WS_2 (on-off ratio of 10^6) (73) or MoS_2 (on-off ratio of 10^3 to 10^4 , probably because of the presence of impurity bands) (70). In addition to logic applications, tunneling in van der Waals heterostructures was exploited for memory devices (74) with a floating gate, logic circuits (75), radio-frequency oscillators (72), and resonant tunneling diodes (76).

Interaction with light

Optoelectronic devices based on graphene (77) as well as other 2D materials (78) have been studied intensively. However, graphene photodetectors typically have low responsivity, which is a consequence of low adsorption coefficient. Such issues are eliminated when other 2D materials are used for such purposes. Thus, TMDCs (78), GaS (79), InSe (80), black phosphorus (81), and other materials (82) have been used as photodetectors (83) in photodiode or photoconductor regimes. The advantages of using such materials are the large DOS (which guarantees large optical adsorption), the materials' flexibility, and the possibility of local gating, which allows the creation of p-n junctions (84). Furthermore, the band gap in such materials often depends on the number of layers (3), which allows one to control the spectral response in such devices.

Van der Waals heterostructures for photovoltaic applications

Still, even larger opportunities open up when such materials are combined. Combinations of graphene (as a channel material) and TMDCs (as light-sensitive material, where trapped charges are controlled by illumination) allow creation of simple and efficient phototransistors (85).

Combining materials with different work functions can lead to photoexcited electrons and holes accumulated in different layers, giving rise to indirect excitons [e.g., as has been observed for the pairs $\text{MoS}_2/\text{WSe}_2$ (86) and $\text{MoSe}_2/\text{WSe}_2$ (87) (Fig. 5, E and F)]. Such excitons typically have long lifetimes, and their binding energy could be tuned by controlling the distance between the semiconductor layers.

If p- and n-doped materials are used in such devices, then atomically sharp p-n junctions can be created (88, 89). Such devices are extremely efficient in carrier separation, so they demonstrate very high quantum efficiency [for instance, GaTe/MoS_2 devices had external quantum efficiencies of >60% (88)]. Furthermore, their performance can be tuned externally by gate voltage, as has been demonstrated for black phosphorus/ MoS_2 heterostructures (90).

Even more efficient photovoltaic devices can be created by combining thin layers of TMDCs (91) or metal chalcogenides (92) with graphene. By sandwiching the photosensitive material between graphene electrodes, one can achieve very efficient photocarrier extraction from the device into graphene electrodes (which typically form good ohmic contacts with the TMDCs and serve as a transparent electrode as well). Because these structures are typically symmetric (Fig. 5G), one needs to create an electric field inside the TMDC to produce efficient carrier separation by bias, external gating (because the electric field is not fully screened by graphene due to its low DOS), or different doping of the two graphene layers.

Light-emitting diodes

The p-n junctions described above can be operated in the regime of electrical injection of the charge carriers, which leads to electron-hole recombination and light emission (89). However, such arrangement is limited by the requirements of synthesizing p- and n-type materials, which have not yet been demonstrated for all 2D crystals. Furthermore, the resistance of the junction is comparable to the resistances of the p and n electrodes, which makes it hard to control the current distribution.

A more straightforward arrangement is the carrier injection from highly conductive transparent electrodes directly into the 2D material in a vertical structure. Such a scheme, however, requires careful control of the dwell time of the injected electrons and holes in the semiconductor crystal, because photoemission is a slow process in comparison with the characteristic time required to penetrate the junction between graphene and the semiconductor. The dwell time can be controlled by introducing additional tunnel barriers (Fig. 5H). Thus, two to three layers of hBN have

been used (93) to increase the time electrons and holes spend inside the monolayer TMDC, allowing their radiative recombination. Devices based on WSe₂ are particularly efficient: Their quantum efficiency increases with increasing temperature and injection current, reaching 20% at room temperature (94). One can increase the quantum efficiency of such structures by placing several layers of TMDCs in series (93) (Fig. 5I).

Plasmonic devices

Plasmons in graphene attract a lot of attention because it is possible to tune their frequency by changing the carrier concentration and, thus, the plasmonic frequency (95). Simultaneously, plasmonic and phonon-polaritonic properties have

been studied in other 2D materials. For instance, hBN has polar dielectric properties, so it supports surface phonon polaritons with very low optical losses (96).

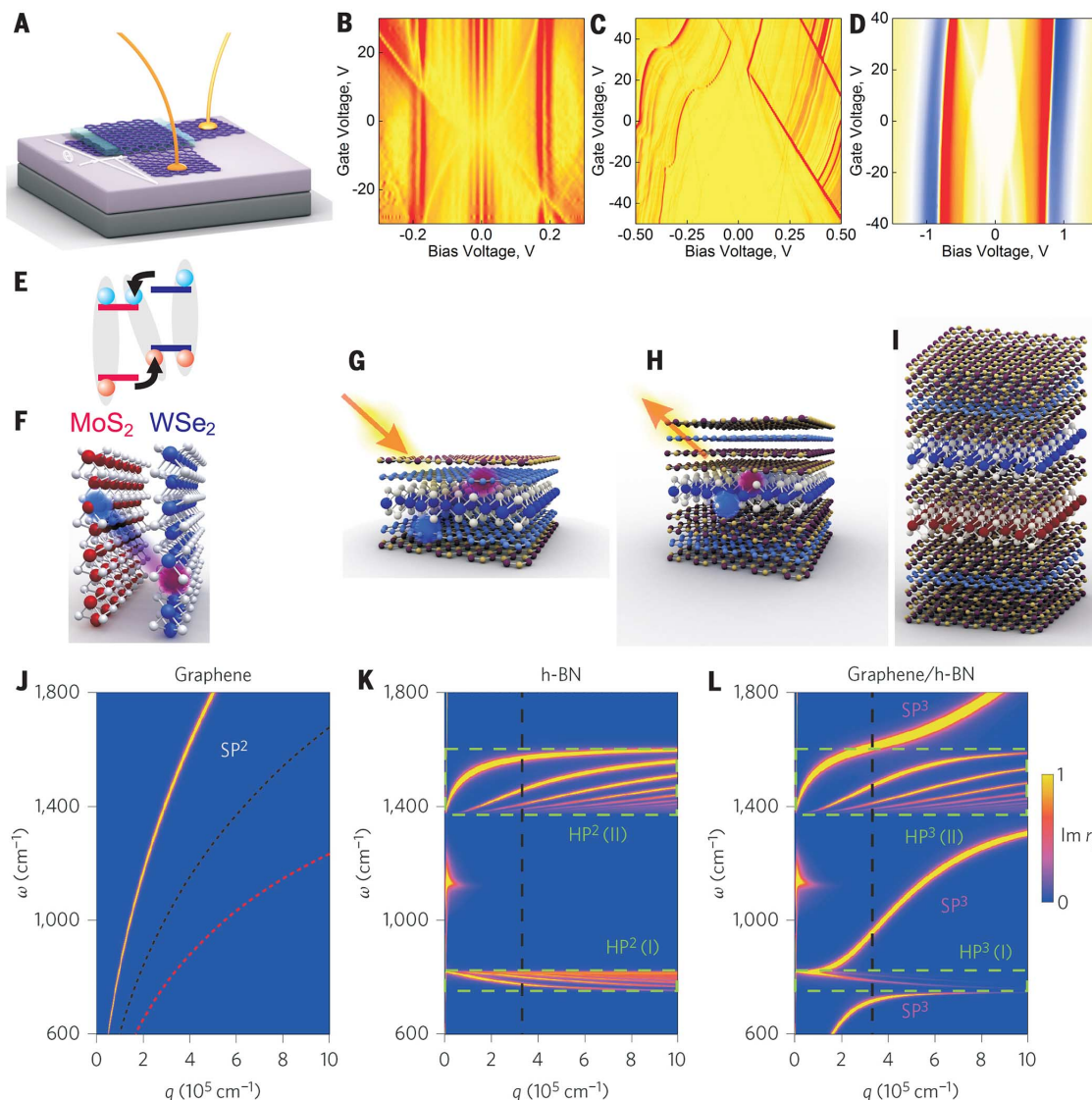
A number of new polaritonic effects can be seen in van der Waals heterostructures. Encapsulation of graphene with hBN allows one to eliminate the scattering of graphene plasmons with impurities, increasing their inverse damping ratio by a factor of 5 in comparison with bare graphene (97). By sandwiching several graphene layers separated by hBN spacers, one can hybridize plasmonic modes in such multilayers, which can be further controlled with external gate voltage (98).

In such heterostructures, it is possible to enter a regime where the plasmon polaritons in gra-

phene and the phonon polaritons in hBN coexist [Fig. 5, J to L; adapted from (99)]. Strong coupling between the two leads to formation of the new collective modes: plasmon-phonon polaritons (100). Both the amplitude and the wavelength of the new collective modes can be controlled by gating graphene.

In aligned graphene/hBN heterostructures, the formation of the moiré pattern provides further modification of the graphene plasmonic spectrum. Zone folding results in the formation of the secondary Dirac points (5–8, 65) (Fig. 4M), which allows a new type of vertical optical transition. Such transitions are immediately reflected in the modified damping factor, which exhibits a maximum at such Fermi energies (101). It has also

Fig. 5. Electronic and optoelectronic applications of van der Waals heterostructures. (A to D) Tunneling in graphene/hBN/graphene tunnel transistors. (A) Schematic representation of a graphene tunneling device. Graphene electrodes are shown in dark purple, and the hBN tunneling barrier is light blue. The electrodes can be aligned with respect to each other. (B) d^2I/dV_b^2 map of phonon-assisted tunneling. Color scale: yellow to red corresponds to 0 to $3.8 \times 10^{-5} \text{ ohm}^{-1} \text{ V}^{-1}$. (C) dI/dV_b map of resonant tunneling due to the presence of impurities in the hBN tunnel layer. Color scale: yellow to red corresponds to 0 to $7 \times 10^{-8} \text{ ohm}^{-1}$. (D) dI/dV_b map of resonant tunneling with momentum conservation due to crystallographic alignment of two graphene electrodes. Blue coloring denotes the range of voltages where the negative differential conductivity is observed. Color scale: blue to white to red corresponds to -6×10^{-6} to 0 to $6 \times 10^{-6} \text{ ohm}^{-1}$. (E and F) Indirect excitons in a MoS₂/WSe₂ heterostructure. Photoexcited electrons from WSe₂ are accumulated in MoS₂. Photoexcited holes from MoS₂ are accumulated in WSe₂. (G) TMDCs (large blue and white spheres) sandwiched between two graphene electrodes (small light-blue spheres) for photovoltaic applications. Photocarriers generated in TMDCs are separated into the opposite graphene electrodes due to an electric field created by external gating (not shown). The structure can be encapsulated in hBN (purple and yellow spheres). (H and I) Vertical light-emitting diode heterostructures.



Photoexcited electrons from WSe₂ are accumulated in MoS₂. Photoexcited holes from MoS₂ are accumulated in WSe₂. (G) TMDCs (large blue and white spheres) sandwiched between two graphene electrodes (small light-blue spheres) for photovoltaic applications. Photocarriers generated in TMDCs are separated into the opposite graphene electrodes due to an electric field created by external gating (not shown). The structure can be encapsulated in hBN (purple and yellow spheres). (H and I) Vertical light-emitting diode heterostructures.

hBN barriers increase the dwell time of the electron and hole in the TMDC, allowing their radiative recombination. Multiple quantum wells, formed by different materials, can be used in such structures (I). Coloring of the atoms is the same as in (F) and (G). (J to L) Polaritonic dispersions of graphene, hBN, and a graphene/hBN heterostructure. q , polariton momentum; ω , polariton frequency; r_p , the imaginary part of the reflectivity.

been predicted that new plasmonic modes with carrier density dependence characteristic of parabolic electronic bands should appear in the vicinity of the van Hove singularities of the reconstructed spectrum (101) (Fig. 4M).

Assembling van der Waals heterostructures in liquid and from liquid-phase-exfoliated 2D materials

A very powerful method of preparing graphene, which can also be extended to other materials, is liquid-phase exfoliation (102). Ink formulation based on such suspensions led to the development of graphene-based printed electronics (103). However, many applications would strongly benefit from properties beyond the capabilities of graphene inks. Thus, high thermal conductivity combined with dielectric property can be delivered by hBN, and optoelectronic capabilities can be delivered by inks of 2D semiconductors.

The ability to print combinations of such materials opens the door for low-cost fabrication of various devices (104). Planar (105) and vertical (106) photovoltaic devices based on TMDCs, as well as planar (107) and tunneling transistors (106) based on graphene and hBN, have recently been demonstrated.

By solution synthesis of 2D crystals or by controlling the charge on individual flakes in suspensions, heterostructures can be formed directly in the liquid phase (108) and can be used for energy applications. For instance, MoSe_2 /graphene structures have been used for Li-ion battery applications (109). Similar heterostructures have also been used for catalytic applications (110).

Growing van der Waals heterostructures

Direct growth methods such as CVD are promising techniques for scalable manufacturing of van der Waals heterostructures (111). Such techniques can be grouped as follows: (i) sequential CVD growth of 2D crystals on top of mechanically transferred or grown 2D materials, (ii) direct growth of TMDC heterostructures by vapor-solid reactions, and (iii) van der Waals epitaxy. State-of-the-art CVD, direct growth, and van der Waals epitaxy methods have already enabled the growth of many vertical heterostructures, such as graphene/hBN (112–116), MoS_2 /graphene (117–120), GaSe/graphene (121), MoS_2 /hBN (122, 123), WS_2 /hBN (124), MoTe_2 / MoS_2 (125), WS_2 / MoS_2 (126), VSe_2 /GeSe₂ (127), MoSe_2 /Bi₂Se₃ (128), MoSe_2 /HfSe₂ (129), MoS_2 /WSe₂/graphene, and WSe₂/MoSe₂/graphene (76).

In situ CVD growth of encapsulated graphene in a hBN/graphene/hBN heterostructure was an important achievement because it demonstrated the scalability of high-mobility graphene-based field-effect transistors (116). Also, some of the TMDC heterostructures can be grown directly in a single-step process: A WS_2 /MoSe₂ heterobilayer was grown on a SiO_2 /Si substrate at 850°C from precursors (W, S, MoO₃) placed in the growth tube [Fig. 6A; adapted from (126)]. Because of the difference in the growth rates of MoS₂ and WS₂, the formation of a $\text{Mo}_x\text{W}_{1-x}\text{S}_2$ alloy is suppressed. A clean interface enabled a band alignment of

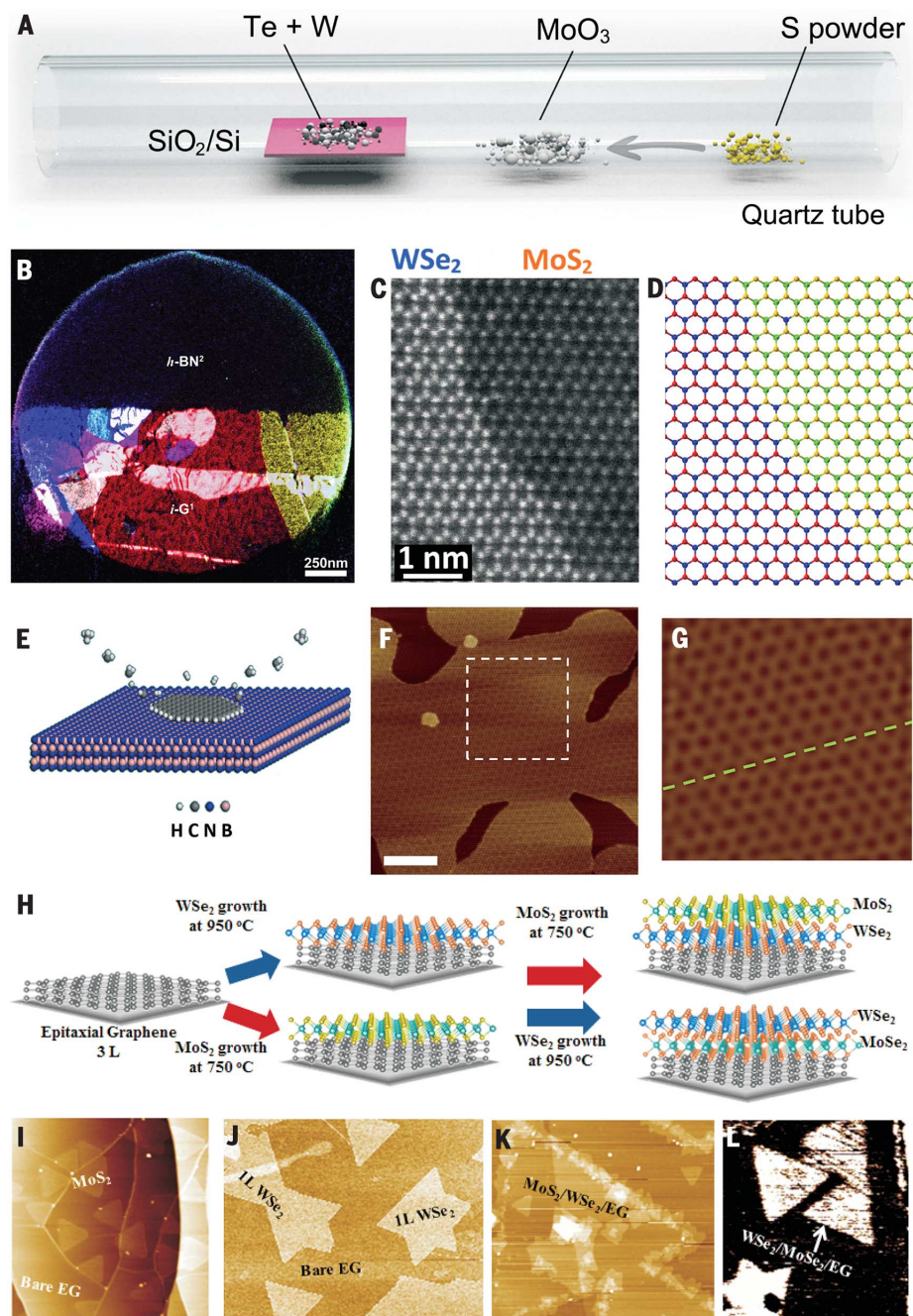


Fig. 6. Van der Waals epitaxy of vertical and in-plane heterostructures. (A) Schematic of the growth process of vertically stacked and in-plane WS_2 /MoSe₂ heterostructures. (B) False-color dark-field TEM image of a suspended hBN/graphene in-plane heterostructure. (C and D) High-resolution scanning transmission electron microscopy image and an atomic model of a WSe_2 /MoSe₂ in-plane heterostructure. (E) Schematics of vertical van der Waals heteroepitaxy of graphene on hBN. (F and G) (F) Moiré pattern of a graphene/hBN heterostructure as observed in tapping-mode AFM and (G) high-pass-filtered inverse fast Fourier transform of the dashed square region in (F). Scale bar in (F), 100 nm. (H) Schematics of the growth of MoS_2 /WSe₂/graphene (top) and WSe₂/MoSe₂/graphene (bottom). Synthesis of both three-component heterostructures begins by growing three layers (3L) of epitaxial graphene (EG), followed by metal-organic CVD growth of either MoS_2 (I) or WSe_2 (J). Then, another TMDC layer is grown by vapor transfer of either MoS_2 (K) or WSe_2 (L). (I to K) AFM images of MoS_2 /graphene, WSe_2 /graphene, and MoS_2 /WSe₂/graphene vertical heterostructures, respectively. (L) Conductive AFM image of a WSe_2 /MoSe₂/graphene heterostructure. Color scale: black to white corresponds to 0 to 100 pA. Due to Se-S ion exchange, a layer of MoSe_2 forms from the original MoS_2 layer.

the two constituent layers, which led to the observation of indirect excitons in the WS_2/MoS_2 heterostructure.

Van der Waals epitaxy

Van der Waals epitaxy was introduced more than 30 years ago with the growth of a NbSe_2 monolayer on a cleaved face of MoS_2 bulk crystal (130). This work also led to the successful growth of monolayer MoSe_2 on SnS_2 (131), as well as growth of a two-component heterostructure of monolayer NbSe_2 /trilayer MoSe_2 on mica (132).

To grow graphene on hBN, Yang *et al.* used plasma to break down precursor methane molecules (48), after which growth occurred at 500°C over the course of 2 to 3 hours on hBN crystals mechanically exfoliated on a SiO_2/Si substrate. Van der Waals interactions during epitaxial growth defined the preferential growth directions so that graphene crystals were aligned to the hBN substrate [Fig. 6, E to G; adapted from (48)].

Mechanically exfoliated hBN has also served as a substrate for CVD-based van der Waals epitaxy of a rotationally commensurate MoS_2/hBN heterostructure (122). Another example of van der Waals epitaxy is the growth of high-quality wafer-scale $\text{MoSe}_2/\text{Bi}_2\text{Se}_3$ heterostructures on the low-cost dielectric substrate AlN/Si in ultrahigh vacuum conditions (128).

Graphene is also a good substrate for van der Waals epitaxy: Grown WSe_2 /graphene heterostructures show an atomically sharp interface and nearly perfect crystallographic orientation between graphene and WSe_2 , despite a large (23%) lattice mismatch (133). Few-layer MoS_2 and hBN structures were also grown using epitaxial graphene as a growth substrate (117, 134). Recently, monolayers of WSe_2 and MoS_2 were grown on free-standing CVD graphene (135). TMDC crystals were also explored as substrates for epitaxy when a MoTe_2 monolayer was grown on a bulk MoS_2 substrate (125).

Finally, van der Waals epitaxy can be repeated several times to grow complex multicomponent heterostructures, such as atomically thin resonant tunneling diodes based on $\text{MoS}_2/\text{WSe}_2$ /graphene and $\text{WSe}_2/\text{MoSe}_2$ /graphene [Fig. 6, H to L; adapted from (76)]. To this end, an epitaxial graphene trilayer was used as a substrate to grow monolayers of either MoS_2 (at 750°C) or WSe_2 (at 850°C) via powder vaporization or metal-organic CVD processes. Subsequently, a second TMDC layer (WSe_2 or MoS_2) was grown on top of the initially grown heterostructure.

Lateral heterostructures

Lateral heterostructures can also be grown by a variety of methods. Thus, CVD-grown graphene was lithographically patterned and etched away, and hBN was grown via CVD, forming lateral 1D heterojunctions [Fig. 6B; adapted from (136)]. Beyond graphene and hBN, lateral heterostructures based on 2D TMDCs can be disruptive for integrated optoelectronic devices. Although direct growth favors TMDC alloys because of a similar chemistry and a small lattice mismatch between different TMDCs (137), two-step epitaxial growth

of a $\text{MoS}_2/\text{WSe}_2$ lateral heterostructure was recently demonstrated [Fig. 6, C and D; adapted from (138)]. To avoid alloying during growth, two separate temperature regimes were used (138). The atomically sharp $\text{WSe}_2/\text{MoS}_2$ heterojunction has a depletion width of ≈ 300 nm due to the potential difference between the MoS_2 and WSe_2 regions.

Lateral heterostructures of MoS_2/WS_2 and $\text{WSe}_2/\text{MoSe}_2$ were grown directly by controlling the growth temperature at $\sim 650^\circ\text{C}$ (126). Growth at relatively low temperatures was facilitated by either introducing tellurium into the CVD process (126) or using perylene-based growth promoters (139). The use of growth-promoting perylene-based aromatic molecules was recently extended to stitch together largely dissimilar 2D materials.

Conclusion

The family of 2D crystals is continuously growing, both in terms of variety and number of materials, and it looks like this process is only beginning. Almost every new 2D material possesses unusual physical properties. The 2D physics (e.g., KT transitions) in such materials is just starting to emerge. Still, we argue that the most interesting phenomena can be realized in van der Waals heterostructures, which now can be mechanically assembled or grown by a variety of techniques. Among the unsolved problems is the control of surface reconstruction, charge transfers, and built-in electric fields in such heterostructures. The standard band diagrams with quasi-electric fields are not a useful concept in 2D heterostructures; therefore, a new framework must be developed.

REFERENCES AND NOTES

- K. S. Novoselov *et al.*, Two-dimensional atomic crystals. *Proc. Natl. Acad. Sci. U.S.A.* **102**, 10451–10453 (2005). doi: [10.1073/pnas.0502848102](https://doi.org/10.1073/pnas.0502848102); pmid: [16027370](https://pubmed.ncbi.nlm.nih.gov/16027370/)
- K. S. Novoselov *et al.*, Electric field effect in atomically thin carbon films. *Science* **306**, 666–669 (2004). doi: [10.1126/science.1102896](https://doi.org/10.1126/science.1102896); pmid: [15499015](https://pubmed.ncbi.nlm.nih.gov/15499015/)
- K. F. Mak, C. Lee, J. Hone, J. Shan, T. F. Heinz, Atomically thin MoS_2 : A new direct-gap semiconductor. *Phys. Rev. Lett.* **105**, 136805 (2010). doi: [10.1103/PhysRevLett.105.136805](https://doi.org/10.1103/PhysRevLett.105.136805); pmid: [21230799](https://pubmed.ncbi.nlm.nih.gov/21230799/)
- H. Liu *et al.*, Phosphorene: An unexplored 2D semiconductor with a high hole mobility. *ACS Nano* **8**, 4033–4041 (2014). doi: [10.1021/nn501226z](https://doi.org/10.1021/nn501226z); pmid: [24655084](https://pubmed.ncbi.nlm.nih.gov/24655084/)
- M. Yankowitz *et al.*, Emergence of superlattice Dirac points in graphene on hexagonal boron nitride. *Nat. Phys.* **8**, 382–386 (2012). doi: [10.1038/nphys2272](https://doi.org/10.1038/nphys2272)
- L. A. Ponomarenko *et al.*, Cloning of Dirac fermions in graphene superlattices. *Nature* **497**, 594–597 (2013). doi: [10.1038/nature12187](https://doi.org/10.1038/nature12187); pmid: [23676678](https://pubmed.ncbi.nlm.nih.gov/23676678/)
- C. R. Dean *et al.*, Hofstadter's butterfly and the fractal quantum Hall effect in moiré superlattices. *Nature* **497**, 598–602 (2013). doi: [10.1038/nature12186](https://doi.org/10.1038/nature12186); pmid: [23676673](https://pubmed.ncbi.nlm.nih.gov/23676673/)
- B. Hunt *et al.*, Massive Dirac fermions and Hofstadter butterfly in a van der Waals heterostructure. *Science* **340**, 1427–1430 (2013). doi: [10.1126/science.1237240](https://doi.org/10.1126/science.1237240); pmid: [23686343](https://pubmed.ncbi.nlm.nih.gov/23686343/)
- G. L. Yu *et al.*, Hierarchy of Hofstadter states and replica quantum Hall ferromagnetism in graphene superlattices. *Nat. Phys.* **10**, 525–529 (2014). doi: [10.1038/nphys2979](https://doi.org/10.1038/nphys2979)
- C. R. Woods *et al.*, Commensurate-incommensurate transition in graphene on hexagonal boron nitride. *Nat. Phys.* **10**, 451–456 (2014). doi: [10.1038/nphys2954](https://doi.org/10.1038/nphys2954)
- A. Avsar *et al.*, Spin-orbit proximity effect in graphene. *Nat. Commun.* **5**, 4875 (2014). doi: [10.1038/ncomms5875](https://doi.org/10.1038/ncomms5875); pmid: [25255743](https://pubmed.ncbi.nlm.nih.gov/25255743/)
- Z. Wang *et al.*, Strong interface-induced spin-orbit interaction in graphene on WS_2 . *Nat. Commun.* **6**, 8339 (2015). doi: [10.1038/ncomms9339](https://doi.org/10.1038/ncomms9339); pmid: [26391068](https://pubmed.ncbi.nlm.nih.gov/26391068/)
- A. Carvalho, R. M. Ribeiro, A. H. Castro Neto, Band nesting and the optical response of two-dimensional semiconducting transition metal dichalcogenides. *Phys. Rev. B* **88**, 115205 (2013). doi: [10.1103/PhysRevB.88.115205](https://doi.org/10.1103/PhysRevB.88.115205)
- A. S. Rodin, L. C. Gomes, A. Carvalho, A. H. Castro Neto, Valley physics in tin (II) sulfide. *Phys. Rev. B* **93**, 045431 (2016). doi: [10.1103/PhysRevB.93.045431](https://doi.org/10.1103/PhysRevB.93.045431)
- L. C. Gomes, S. S. Alexandre, H. Chacham, R. W. Nunes, Stability of edges and extended defects on boron nitride and graphene monolayers: The role of chemical environment. *J. Phys. Chem. C* **117**, 11770–11779 (2013). doi: [10.1021/jp400420m](https://doi.org/10.1021/jp400420m)
- H. Chen, Y. Li, L. Huang, J. B. Li, Intrinsic defects in gallium sulfide monolayer: A first-principles study. *RSC Advances* **5**, 50883–50889 (2015). doi: [10.1039/C5RA08329J](https://doi.org/10.1039/C5RA08329J)
- D. V. Rybkovskiy, A. V. Osadchey, E. D. Obraztsova, Transition from parabolic to ring-shaped valence band maximum in few-layer GaS , GaSe , and InSe . *Phys. Rev. B* **90**, 235302 (2014). doi: [10.1103/PhysRevB.90.235302](https://doi.org/10.1103/PhysRevB.90.235302)
- J. A. Wilson, A. D. Yoffe, The transition metal dichalcogenides discussion and interpretation of the observed optical, electrical and structural properties. *Adv. Phys.* **18**, 193–335 (1969). doi: [10.1080/00018736900101307](https://doi.org/10.1080/00018736900101307)
- A. H. Castro Neto, Charge density wave, superconductivity, and anomalous metallic behavior in 2D transition metal dichalcogenides. *Phys. Rev. Lett.* **86**, 4382–4385 (2001). doi: [10.1103/PhysRevLett.86.4382](https://doi.org/10.1103/PhysRevLett.86.4382); pmid: [11328180](https://pubmed.ncbi.nlm.nih.gov/11328180/)
- T. Valla *et al.*, Charge-density-wave-induced modifications to the quasiparticle self-energy in 2H- TaSe_2 . *Phys. Rev. Lett.* **85**, 4759–4762 (2000). doi: [10.1103/PhysRevLett.85.4759](https://doi.org/10.1103/PhysRevLett.85.4759); pmid: [11082645](https://pubmed.ncbi.nlm.nih.gov/11082645/)
- H. F. Hess, R. B. Robinson, J. V. Waszczak, STM spectroscopy of vortex cores and the flux lattice. *Physica B* **169**, 422–431 (1991). doi: [10.1016/0921-4526\(91\)90262-D](https://doi.org/10.1016/0921-4526(91)90262-D)
- L. J. Li *et al.*, Controlling many-body states by the electric-field effect in a two-dimensional material. *Nature* **529**, 185–189 (2016). doi: [10.1038/nature16175](https://doi.org/10.1038/nature16175); pmid: [26700810](https://pubmed.ncbi.nlm.nih.gov/26700810/)
- P. C. Hohenberg, Existence of long-range order in one and two dimensions. *Phys. Rev.* **158**, 383–386 (1967). doi: [10.1103/PhysRev.158.383](https://doi.org/10.1103/PhysRev.158.383)
- P. Minnhagen, The two-dimensional Coulomb gas, vortex unbinding, and superfluid-superconducting films. *Rev. Mod. Phys.* **59**, 1001–1066 (1987). doi: [10.1103/RevModPhys.59.1001](https://doi.org/10.1103/RevModPhys.59.1001)
- J. Shang *et al.*, Observation of excitonic fine structure in a 2D transition-metal dichalcogenide semiconductor. *ACS Nano* **9**, 647–655 (2015). doi: [10.1021/nn5059908](https://doi.org/10.1021/nn5059908); pmid: [25560634](https://pubmed.ncbi.nlm.nih.gov/25560634/)
- K. F. Mak *et al.*, Tightly bound trions in monolayer MoS_2 . *Nat. Mater.* **12**, 207–211 (2013). doi: [10.1038/nmat3505](https://doi.org/10.1038/nmat3505); pmid: [23202371](https://pubmed.ncbi.nlm.nih.gov/23202371/)
- B. Zhu, X. Chen, X. Cui, Exciton binding energy of monolayer WS_2 . *Sci. Rep.* **5**, 9218 (2015). doi: [10.1038/srep09218](https://doi.org/10.1038/srep09218); pmid: [25783023](https://pubmed.ncbi.nlm.nih.gov/25783023/)
- A. Chernikov *et al.*, Exciton binding energy and nonhydrogenic Rydberg series in monolayer WS_2 . *Phys. Rev. Lett.* **113**, 076802 (2014). doi: [10.1103/PhysRevLett.113.076802](https://doi.org/10.1103/PhysRevLett.113.076802); pmid: [25170725](https://pubmed.ncbi.nlm.nih.gov/25170725/)
- Z. Ye *et al.*, Probing excitonic dark states in single-layer tungsten disulphide. *Nature* **513**, 214–218 (2014). doi: [10.1038/nature13734](https://doi.org/10.1038/nature13734); pmid: [25162523](https://pubmed.ncbi.nlm.nih.gov/25162523/)
- D. Xiao, G.-B. Liu, W. Feng, X. Xu, W. Yao, Coupled spin and valley physics in monolayers of MoS_2 and other group-VI dichalcogenides. *Phys. Rev. Lett.* **108**, 196802 (2012). doi: [10.1103/PhysRevLett.108.196802](https://doi.org/10.1103/PhysRevLett.108.196802); pmid: [23003071](https://pubmed.ncbi.nlm.nih.gov/23003071/)
- H. Zeng, J. Dai, W. Yao, D. Xiao, X. Cui, Valley polarization in MoS_2 monolayers by optical pumping. *Nat. Nanotechnol.* **7**, 490–493 (2012). doi: [10.1038/nnano.2012.95](https://doi.org/10.1038/nnano.2012.95); pmid: [22706701](https://pubmed.ncbi.nlm.nih.gov/22706701/)
- T. Cao *et al.*, Valley-selective circular dichroism of monolayer molybdenum disulphide. *Nat. Commun.* **3**, 887 (2012). doi: [10.1038/ncomms1882](https://doi.org/10.1038/ncomms1882); pmid: [22673914](https://pubmed.ncbi.nlm.nih.gov/22673914/)
- K. F. Mak, K. He, J. Shan, T. F. Heinz, Control of valley polarization in monolayer MoS_2 by optical helicity. *Nat. Nanotechnol.* **7**, 494–498 (2012). doi: [10.1038/nnano.2012.96](https://doi.org/10.1038/nnano.2012.96); pmid: [22706698](https://pubmed.ncbi.nlm.nih.gov/22706698/)
- A. M. Jones *et al.*, Optical generation of excitonic valley coherence in monolayer WSe_2 . *Nat. Nanotechnol.* **8**, 634–638 (2013). doi: [10.1038/nnano.2013.151](https://doi.org/10.1038/nnano.2013.151); pmid: [23934096](https://pubmed.ncbi.nlm.nih.gov/23934096/)
- D. Xiao, W. Yao, Q. Niu, Valley-contrasting physics in graphene: Magnetic moment and topological transport.

- Phys. Rev. Lett.* **99**, 236809 (2007). doi: [10.1103/PhysRevLett.99.236809](https://doi.org/10.1103/PhysRevLett.99.236809); pmid: [18233399](https://pubmed.ncbi.nlm.nih.gov/18233399/)
36. K. F. Mak, K. L. McGill, J. Park, P. L. McEuen, The valley Hall effect in MoS₂ transistors. *Science* **344**, 1489–1492 (2014). doi: [10.1126/science.1250140](https://doi.org/10.1126/science.1250140); pmid: [24970080](https://pubmed.ncbi.nlm.nih.gov/24970080/)
 37. L. Li et al., Black phosphorus field-effect transistors. *Nat. Nanotechnol.* **9**, 372–377 (2014). doi: [10.1038/nnano.2014.35](https://doi.org/10.1038/nnano.2014.35); pmid: [24584274](https://pubmed.ncbi.nlm.nih.gov/24584274/)
 38. J. Qiao, X. Kong, Z. X. Hu, F. Yang, W. Ji, High-mobility transport anisotropy and linear dichroism in few-layer black phosphorus. *Nat. Commun.* **5**, 4475 (2014). doi: [10.1038/ncomms5475](https://doi.org/10.1038/ncomms5475); pmid: [25042376](https://pubmed.ncbi.nlm.nih.gov/25042376/)
 39. R. Fei et al., Enhanced thermoelectric efficiency via orthogonal electrical and thermal conductances in phosphorene. *Nano Lett.* **14**, 6393–6399 (2014). doi: [10.1021/nl502865s](https://doi.org/10.1021/nl502865s); pmid: [25254626](https://pubmed.ncbi.nlm.nih.gov/25254626/)
 40. L. C. Gomes, A. Carvalho, Phosphorene analogues: Isoelectronic two-dimensional group-IV monochalcogenides with orthorhombic structure. *Phys. Rev. B* **92**, 085406 (2015). doi: [10.1103/PhysRevB.92.085406](https://doi.org/10.1103/PhysRevB.92.085406)
 41. L. C. Gomes, A. Carvalho, A. H. Castro Neto, Enhanced piezoelectricity and modified dielectric screening of two-dimensional group-IV monochalcogenides. *Phys. Rev. B* **92**, 214103 (2015). doi: [10.1103/PhysRevB.92.214103](https://doi.org/10.1103/PhysRevB.92.214103)
 42. V. Zolyomi, N. D. Drummond, V. I. Fal'ko, Band structure and optical transitions in atomic layers of hexagonal gallium chalcogenides. *Phys. Rev. B* **87**, 195403 (2013). doi: [10.1103/PhysRevB.87.195403](https://doi.org/10.1103/PhysRevB.87.195403)
 43. V. Zolyomi, N. D. Drummond, V. I. Fal'ko, Electrons and phonons in single layers of hexagonal indium chalcogenides from ab initio calculations. *Phys. Rev. B* **89**, 205416 (2014). doi: [10.1103/PhysRevB.89.205416](https://doi.org/10.1103/PhysRevB.89.205416)
 44. D. J. Late et al., GaS and GaSe ultrathin layer transistors. *Adv. Mater.* **24**, 3549–3554 (2012). doi: [10.1002/adma.201201361](https://doi.org/10.1002/adma.201201361); pmid: [22678832](https://pubmed.ncbi.nlm.nih.gov/22678832/)
 45. P. Hu, Z. Wen, L. Wang, P. Tan, K. Xiao, Synthesis of few-layer GaSe nanosheets for high performance photodetectors. *ACS Nano* **6**, 5988–5994 (2012). doi: [10.1021/nl300889c](https://doi.org/10.1021/nl300889c); pmid: [22676041](https://pubmed.ncbi.nlm.nih.gov/22676041/)
 46. S. Wu et al., <http://arxiv.org/abs/1409.4733> (2014).
 47. C. R. Dean et al., Boron nitride substrates for high-quality graphene electronics. *Nat. Nanotechnol.* **5**, 722–726 (2010). doi: [10.1038/nnano.2010.172](https://doi.org/10.1038/nnano.2010.172); pmid: [20729834](https://pubmed.ncbi.nlm.nih.gov/20729834/)
 48. W. Yang et al., Epitaxial growth of single-domain graphene on hexagonal boron nitride. *Nat. Mater.* **12**, 792–797 (2013). doi: [10.1038/nmat3695](https://doi.org/10.1038/nmat3695); pmid: [23852399](https://pubmed.ncbi.nlm.nih.gov/23852399/)
 49. R. J. Cava et al., Superconductivity near 70 K in a new family of layered copper oxides. *Nature* **336**, 211–214 (1988). doi: [10.1038/336211a0](https://doi.org/10.1038/336211a0)
 50. K. Takada et al., Superconductivity in two-dimensional CoO₂ layers. *Nature* **422**, 53–55 (2003). doi: [10.1038/nature01450](https://doi.org/10.1038/nature01450); pmid: [12621429](https://pubmed.ncbi.nlm.nih.gov/12621429/)
 51. A. Ziletti et al., Phosphorene oxides: Bandgap engineering of phosphorene by oxidation. *Phys. Rev. B* **91**, 085407 (2015). doi: [10.1103/PhysRevB.91.085407](https://doi.org/10.1103/PhysRevB.91.085407)
 52. J. Lu et al., Bandgap engineering of phosphorene by laser oxidation toward functional 2D materials. *ACS Nano* **9**, 10411–10421 (2015). doi: [10.1021/acs.nano.5b04623](https://doi.org/10.1021/acs.nano.5b04623); pmid: [26364647](https://pubmed.ncbi.nlm.nih.gov/26364647/)
 53. M. A. Green, A. Ho-Baillie, H. J. Snaith, The emergence of perovskite solar cells. *Nat. Photonics* **8**, 506–514 (2014). doi: [10.1038/nphoton.2014.134](https://doi.org/10.1038/nphoton.2014.134)
 54. A. K. Geim, I. V. Grigorieva, van der Waals heterostructures. *Nature* **499**, 419–425 (2013). doi: [10.1038/nature12385](https://doi.org/10.1038/nature12385); pmid: [23887427](https://pubmed.ncbi.nlm.nih.gov/23887427/)
 55. S. J. Haigh et al., Cross-sectional imaging of individual layers and buried interfaces of graphene-based heterostructures and superlattices. *Nat. Mater.* **11**, 764–767 (2012). doi: [10.1038/nmat3386](https://doi.org/10.1038/nmat3386); pmid: [22842512](https://pubmed.ncbi.nlm.nih.gov/22842512/)
 56. L. Wang et al., One-dimensional electrical contact to a two-dimensional material. *Science* **342**, 614–617 (2013). doi: [10.1126/science.1244358](https://doi.org/10.1126/science.1244358); pmid: [24179223](https://pubmed.ncbi.nlm.nih.gov/24179223/)
 57. A. V. Kretinin et al., Electronic properties of graphene encapsulated with different two-dimensional atomic crystals. *Nano Lett.* **14**, 3270–3276 (2014). doi: [10.1021/nl5006542](https://doi.org/10.1021/nl5006542); pmid: [24844319](https://pubmed.ncbi.nlm.nih.gov/24844319/)
 58. G. Giovannetti, P. A. Khomyakov, G. Brocks, P. J. Kelly, J. van den Brink, Substrate-induced band gap in graphene on hexagonal boron nitride: Ab initio density functional calculations. *Phys. Rev. B* **76**, 073103 (2007). doi: [10.1103/PhysRevB.76.073103](https://doi.org/10.1103/PhysRevB.76.073103)
 59. J. Kang, J. Li, S. S. Li, J. B. Xia, L. W. Wang, Electronic structural Moiré pattern effects on MoS₂/MoSe₂ 2D heterostructures. *Nano Lett.* **13**, 5485–5490 (2013). doi: [10.1021/nl4030648](https://doi.org/10.1021/nl4030648); pmid: [24079953](https://pubmed.ncbi.nlm.nih.gov/24079953/)
 60. S. Tongay et al., Tuning interlayer coupling in large-area heterostructures with CVD-grown MoS₂ and WS₂ monolayers. *Nano Lett.* **14**, 3185–3190 (2014). doi: [10.1021/nl500515q](https://doi.org/10.1021/nl500515q); pmid: [24845201](https://pubmed.ncbi.nlm.nih.gov/24845201/)
 61. L. F. Wang et al., Superlubricity of two-dimensional fluorographene/MoS₂ heterostructure: A first-principles study. *Nanotechnology* **25**, 385701 (2014). doi: [10.1088/0957-4484/25/38/385701](https://doi.org/10.1088/0957-4484/25/38/385701); pmid: [25180979](https://pubmed.ncbi.nlm.nih.gov/25180979/)
 62. H. Terrones, F. López-Urías, M. Terrones, Novel hetero-layered materials with tunable direct band gaps by sandwiching different metal disulfides and diselenides. *Sci. Rep.* **3**, 1549 (2013). doi: [10.1038/srep01549](https://doi.org/10.1038/srep01549); pmid: [23528957](https://pubmed.ncbi.nlm.nih.gov/23528957/)
 63. C. H. Lui et al., Observation of interlayer phonon modes in van der Waals heterostructures. *Phys. Rev. B* **91**, 165403 (2015). doi: [10.1103/PhysRevB.91.165403](https://doi.org/10.1103/PhysRevB.91.165403)
 64. L. Y. Li, M. W. Zhao, Structures, energetics, and electronic properties of multifarious stacking patterns for high-buckled and low-buckled silicene on the MoS₂ substrate. *J. Phys. Chem. C* **118**, 19129–19138 (2014). doi: [10.1021/jp5043359](https://doi.org/10.1021/jp5043359)
 65. J. R. Wallbank, A. A. Patel, M. Mucha-Kruczynski, A. K. Geim, V. I. Fal'ko, Generic miniband structure of graphene on a hexagonal substrate. *Phys. Rev. B* **87**, 245408 (2013). doi: [10.1103/PhysRevB.87.245408](https://doi.org/10.1103/PhysRevB.87.245408)
 66. G. L. Yu et al., Interaction phenomena in graphene seen through quantum capacitance. *Proc. Natl. Acad. Sci. U.S.A.* **110**, 3282–3286 (2013). doi: [10.1073/pnas.1300599110](https://doi.org/10.1073/pnas.1300599110); pmid: [23401538](https://pubmed.ncbi.nlm.nih.gov/23401538/)
 67. M. Kuiri et al., Probing 2D black phosphorus by quantum capacitance measurements. *Nanotechnology* **26**, 485704 (2015). doi: [10.1088/0957-4484/26/48/485704](https://doi.org/10.1088/0957-4484/26/48/485704); pmid: [26559656](https://pubmed.ncbi.nlm.nih.gov/26559656/)
 68. R. V. Gorbachev et al., Strong Coulomb drag and broken symmetry in double-layer graphene. *Nat. Phys.* **8**, 896–901 (2012). doi: [10.1038/nphys2441](https://doi.org/10.1038/nphys2441)
 69. G. H. Lee et al., Electron tunneling through atomically flat and ultrathin hexagonal boron nitride. *Appl. Phys. Lett.* **99**, 243114 (2011). doi: [10.1063/1.3662043](https://doi.org/10.1063/1.3662043)
 70. L. Britnell et al., Field-effect tunneling transistor based on vertical graphene heterostructures. *Science* **335**, 947–950 (2012). doi: [10.1126/science.1218461](https://doi.org/10.1126/science.1218461); pmid: [22300848](https://pubmed.ncbi.nlm.nih.gov/22300848/)
 71. F. Amet et al., Tunneling spectroscopy of graphene-boron-nitride heterostructures. *Phys. Rev. B* **85**, 073405 (2012). doi: [10.1103/PhysRevB.85.073405](https://doi.org/10.1103/PhysRevB.85.073405)
 72. A. Mishchenko et al., Twist-controlled resonant tunnelling in graphene/boron nitride/graphene heterostructures. *Nat. Nanotechnol.* **9**, 808–813 (2014). doi: [10.1038/nnano.2014.187](https://doi.org/10.1038/nnano.2014.187); pmid: [25194946](https://pubmed.ncbi.nlm.nih.gov/25194946/)
 73. T. Georgiou et al., Vertical field-effect transistor based on graphene-WS₂ heterostructures for flexible and transparent electronics. *Nat. Nanotechnol.* **8**, 100–103 (2013). doi: [10.1038/nnano.2012.224](https://doi.org/10.1038/nnano.2012.224); pmid: [23263726](https://pubmed.ncbi.nlm.nih.gov/23263726/)
 74. M. S. Choi et al., Controlled charge trapping by molybdenum disulfide and graphene in ultrathin heterostructured memory devices. *Nat. Commun.* **4**, 1624 (2013). doi: [10.1038/ncomms2652](https://doi.org/10.1038/ncomms2652); pmid: [23535645](https://pubmed.ncbi.nlm.nih.gov/23535645/)
 75. H. Yang et al., Graphene barristor, a triode device with a gate-controlled Schottky barrier. *Science* **336**, 1140–1143 (2012). doi: [10.1126/science.1220527](https://doi.org/10.1126/science.1220527); pmid: [22604723](https://pubmed.ncbi.nlm.nih.gov/22604723/)
 76. Y.-C. Lin et al., Atomically thin resonant tunnel diodes built from synthetic van der Waals heterostructures. *Nat. Commun.* **6**, 7311 (2015). doi: [10.1038/ncomms8311](https://doi.org/10.1038/ncomms8311); pmid: [26088295](https://pubmed.ncbi.nlm.nih.gov/26088295/)
 77. F. Bonaccorso, Z. Sun, T. Hasan, A. C. Ferrari, Graphene photonics and optoelectronics. *Nat. Photonics* **4**, 611–622 (2010). doi: [10.1038/nphoton.2010.186](https://doi.org/10.1038/nphoton.2010.186)
 78. Q. H. Wang, K. Kalantar-Zadeh, A. Kis, J. N. Coleman, M. S. Strano, Electronics and optoelectronics of two-dimensional transition metal dichalcogenides. *Nat. Nanotechnol.* **7**, 699–712 (2012). doi: [10.1038/nnano.2012.193](https://doi.org/10.1038/nnano.2012.193); pmid: [23132225](https://pubmed.ncbi.nlm.nih.gov/23132225/)
 79. P. Hu et al., Highly responsive ultrathin GaS nanosheet photodetectors on rigid and flexible substrates. *Nano Lett.* **13**, 1649–1654 (2013). doi: [10.1021/nl400107k](https://doi.org/10.1021/nl400107k); pmid: [23465066](https://pubmed.ncbi.nlm.nih.gov/23465066/)
 80. S. R. Tamalampudi et al., High performance and bendable few-layered InSe photodetectors with broad spectral response. *Nano Lett.* **14**, 2800–2806 (2014). doi: [10.1021/nl500817g](https://doi.org/10.1021/nl500817g); pmid: [24742243](https://pubmed.ncbi.nlm.nih.gov/24742243/)
 81. M. Buscema et al., Fast and broadband photoresponse of few-layer black phosphorus field-effect transistors. *Nano Lett.* **14**, 3347–3352 (2014). doi: [10.1021/nl5008085](https://doi.org/10.1021/nl5008085); pmid: [24821381](https://pubmed.ncbi.nlm.nih.gov/24821381/)
 82. F. N. Xia, H. Wang, D. Xiao, M. Dubey, A. Ramasubramanian, Two-dimensional material nanophotonics. *Nat. Photonics* **8**, 899–907 (2014). doi: [10.1038/nphoton.2014.271](https://doi.org/10.1038/nphoton.2014.271)
 83. F. H. L. Koppens et al., Photodetectors based on graphene, other two-dimensional materials and hybrid systems. *Nat. Nanotechnol.* **9**, 780–793 (2014). doi: [10.1038/nnano.2014.215](https://doi.org/10.1038/nnano.2014.215); pmid: [25286273](https://pubmed.ncbi.nlm.nih.gov/25286273/)
 84. B. W. H. Baugher, H. O. H. Churchill, Y. Yang, P. Jarillo-Herrero, Optoelectronic devices based on electrically tunable p-n diodes in a monolayer dichalcogenide. *Nat. Nanotechnol.* **9**, 262–267 (2014). doi: [10.1038/nnano.2014.25](https://doi.org/10.1038/nnano.2014.25); pmid: [24608231](https://pubmed.ncbi.nlm.nih.gov/24608231/)
 85. K. Roy et al., Graphene-MoS₂ hybrid structures for multifunctional photoresponsive memory devices. *Nat. Nanotechnol.* **8**, 826–830 (2013). doi: [10.1038/nnano.2013.206](https://doi.org/10.1038/nnano.2013.206); pmid: [24141541](https://pubmed.ncbi.nlm.nih.gov/24141541/)
 86. H. Fang et al., Strong interlayer coupling in van der Waals heterostructures built from single-layer chalcogenides. *Proc. Natl. Acad. Sci. U.S.A.* **111**, 6198–6202 (2014). doi: [10.1073/pnas.1405435111](https://doi.org/10.1073/pnas.1405435111); pmid: [24733906](https://pubmed.ncbi.nlm.nih.gov/24733906/)
 87. P. Rivera et al., Observation of long-lived interlayer excitons in monolayer MoSe₂-WSe₂ heterostructures. *Nat. Commun.* **6**, 6242 (2015). doi: [10.1038/ncomms7242](https://doi.org/10.1038/ncomms7242); pmid: [25708612](https://pubmed.ncbi.nlm.nih.gov/25708612/)
 88. F. Wang et al., Tunable GaTe-MoS₂ van der Waals p-n Junctions with novel optoelectronic performance. *Nano Lett.* **15**, 7558–7566 (2015). doi: [10.1021/acs.nanolett.5b03291](https://doi.org/10.1021/acs.nanolett.5b03291); pmid: [26469092](https://pubmed.ncbi.nlm.nih.gov/26469092/)
 89. R. Cheng et al., Electroluminescence and photocurrent generation from atomically sharp WSe₂/MoS₂ heterojunction p-n diodes. *Nano Lett.* **14**, 5590–5597 (2014). doi: [10.1021/nl502075n](https://doi.org/10.1021/nl502075n); pmid: [25157588](https://pubmed.ncbi.nlm.nih.gov/25157588/)
 90. Y. Deng et al., Black phosphorus-monolayer MoS₂ van der Waals heterojunction p-n diode. *ACS Nano* **8**, 8292–8299 (2014). doi: [10.1021/nl5027388](https://doi.org/10.1021/nl5027388); pmid: [25019534](https://pubmed.ncbi.nlm.nih.gov/25019534/)
 91. L. Britnell et al., Strong light-matter interactions in heterostructures of atomically thin films. *Science* **340**, 1311–1314 (2013). doi: [10.1126/science.1235547](https://doi.org/10.1126/science.1235547); pmid: [23641062](https://pubmed.ncbi.nlm.nih.gov/23641062/)
 92. G. W. Mudd et al., High broad-band photoresponsivity of mechanically formed InSe-graphene van der Waals heterostructures. *Adv. Mater.* **27**, 3760–3766 (2015). doi: [10.1002/adma.201500889](https://doi.org/10.1002/adma.201500889); pmid: [25981798](https://pubmed.ncbi.nlm.nih.gov/25981798/)
 93. F. Withers et al., Light-emitting diodes by band-structure engineering in van der Waals heterostructures. *Nat. Mater.* **14**, 301–306 (2015). doi: [10.1038/nmat4205](https://doi.org/10.1038/nmat4205); pmid: [25643033](https://pubmed.ncbi.nlm.nih.gov/25643033/)
 94. F. Withers et al., WSe₂ light-emitting tunneling transistors with enhanced brightness at room temperature. *Nano Lett.* **15**, 8223–8228 (2015). doi: [10.1021/acs.nanolett.5b03740](https://doi.org/10.1021/acs.nanolett.5b03740); pmid: [26555037](https://pubmed.ncbi.nlm.nih.gov/26555037/)
 95. A. N. Grigorenko, M. Polini, K. S. Novoselov, Graphene plasmonics. *Nat. Photonics* **6**, 749–758 (2012). doi: [10.1038/nphoton.2012.262](https://doi.org/10.1038/nphoton.2012.262)
 96. S. Dai et al., Tunable phonon polaritons in atomically thin van der Waals crystals of boron nitride. *Science* **343**, 1125–1129 (2014). doi: [10.1126/science.1246833](https://doi.org/10.1126/science.1246833); pmid: [24604197](https://pubmed.ncbi.nlm.nih.gov/24604197/)
 97. A. Woessner et al., Highly confined low-loss plasmons in graphene-boron nitride heterostructures. *Nat. Mater.* **14**, 421–425 (2015). doi: [10.1038/nmat4169](https://doi.org/10.1038/nmat4169); pmid: [25532073](https://pubmed.ncbi.nlm.nih.gov/25532073/)
 98. K. Zhang et al., Large scale graphene/hexagonal boron nitride heterostructure for tunable plasmonics. *Adv. Funct. Mater.* **24**, 731–738 (2014). doi: [10.1002/adfm.201302009](https://doi.org/10.1002/adfm.201302009)
 99. S. Dai et al., Graphene on hexagonal boron nitride as a tunable hyperbolic metamaterial. *Nat. Nanotechnol.* **10**, 682–686 (2015). doi: [10.1038/nnano.2015.131](https://doi.org/10.1038/nnano.2015.131); pmid: [26098228](https://pubmed.ncbi.nlm.nih.gov/26098228/)
 100. V. W. Brar et al., Hybrid surface-phonon-plasmon polariton modes in graphene/monolayer h-BN heterostructures. *Nano Lett.* **14**, 3876–3880 (2014). doi: [10.1021/nl501096s](https://doi.org/10.1021/nl501096s); pmid: [24874205](https://pubmed.ncbi.nlm.nih.gov/24874205/)
 101. A. Tomadin, F. Guinea, M. Polini, Generation and morphing of plasmons in graphene superlattices. *Phys. Rev. B* **90**, 161406 (2014). doi: [10.1103/PhysRevB.90.161406](https://doi.org/10.1103/PhysRevB.90.161406)
 102. J. N. Coleman et al., Two-dimensional nanosheets produced by liquid exfoliation of layered materials. *Science* **331**, 568–571 (2011). doi: [10.1126/science.1194975](https://doi.org/10.1126/science.1194975); pmid: [21292974](https://pubmed.ncbi.nlm.nih.gov/21292974/)
 103. F. Torrisi et al., Inkjet-printed graphene electronics. *ACS Nano* **6**, 2992–3006 (2012). doi: [10.1021/nl2044609](https://doi.org/10.1021/nl2044609); pmid: [22449258](https://pubmed.ncbi.nlm.nih.gov/22449258/)

104. E. B. Secor, M. C. Hersam, Emerging carbon and post-carbon nanomaterial inks for printed electronics. *J. Phys. Chem. Lett.* **6**, 620–626 (2015). doi: [10.1021/jz502431r](https://doi.org/10.1021/jz502431r); pmid: [26262476](https://pubmed.ncbi.nlm.nih.gov/26262476/)
105. D. J. Finn *et al.*, Inkjet deposition of liquid-exfoliated graphene and MoS₂ nanosheets for printed device applications. *J. Mater. Chem. C* **2**, 925–932 (2014). doi: [10.1039/C3TC31993H](https://doi.org/10.1039/C3TC31993H)
106. F. Withers *et al.*, Heterostructures produced from nanosheet-based inks. *Nano Lett.* **14**, 3987–3992 (2014). doi: [10.1021/nl501355j](https://doi.org/10.1021/nl501355j); pmid: [24871927](https://pubmed.ncbi.nlm.nih.gov/24871927/)
107. J. Zhu *et al.*, Solution-processed dielectrics based on thickness-sorted two-dimensional hexagonal boron nitride nanosheets. *Nano Lett.* **15**, 7029–7036 (2015). doi: [10.1021/acs.nanolett.5b03075](https://doi.org/10.1021/acs.nanolett.5b03075); pmid: [26348822](https://pubmed.ncbi.nlm.nih.gov/26348822/)
108. X. Cai *et al.*, Tuning the surface charge of 2D oxide nanosheets and the bulk-scale production of superlattice-like composites. *J. Am. Chem. Soc.* **137**, 2844–2847 (2015). doi: [10.1021/jacs.5b00317](https://doi.org/10.1021/jacs.5b00317); pmid: [25686203](https://pubmed.ncbi.nlm.nih.gov/25686203/)
109. L. Ma *et al.*, Ultrathin few-layered molybdenum selenide/graphene hybrid with superior electrochemical Li-storage performance. *J. Power Sources* **285**, 274–280 (2015). doi: [10.1016/j.jpowsour.2015.03.120](https://doi.org/10.1016/j.jpowsour.2015.03.120)
110. D. Deng *et al.*, Catalysis with two-dimensional materials and their heterostructures. *Nat. Nanotechnol.* **11**, 218–230 (2016). doi: [10.1038/nnano.2015.340](https://doi.org/10.1038/nnano.2015.340); pmid: [26936816](https://pubmed.ncbi.nlm.nih.gov/26936816/)
111. J. A. Robinson, Growing vertical in the flatland. *ACS Nano* **10**, 42–45 (2016). doi: [10.1021/acsnano.5b08117](https://doi.org/10.1021/acsnano.5b08117); pmid: [26762232](https://pubmed.ncbi.nlm.nih.gov/26762232/)
112. Z. Liu *et al.*, Direct growth of graphene/hexagonal boron nitride stacked layers. *Nano Lett.* **11**, 2032–2037 (2011). doi: [10.1021/nl200464j](https://doi.org/10.1021/nl200464j); pmid: [21488689](https://pubmed.ncbi.nlm.nih.gov/21488689/)
113. W. Gannett *et al.*, Boron nitride substrates for high mobility chemical vapor deposited graphene. *Appl. Phys. Lett.* **98**, 242105 (2011). doi: [10.1063/1.3599708](https://doi.org/10.1063/1.3599708)
114. Z. G. Xu, R. J. Zheng, A. Khanaki, Z. Zuo, J. L. Liu, Direct growth of graphene on in situ epitaxial hexagonal boron nitride flakes by plasma-assisted molecular beam epitaxy. *Appl. Phys. Lett.* **107**, 213103 (2015). doi: [10.1063/1.4936378](https://doi.org/10.1063/1.4936378)
115. C. Zhang *et al.*, Direct growth of large-area graphene and boron nitride heterostructures by a co-segregation method. *Nat. Commun.* **6**, 6519 (2015). doi: [10.1038/ncomms7519](https://doi.org/10.1038/ncomms7519); pmid: [25735443](https://pubmed.ncbi.nlm.nih.gov/25735443/)
116. Q. Wu *et al.*, In situ synthesis of a large area boron nitride/graphene monolayer/boron nitride film by chemical vapor deposition. *Nanoscale* **7**, 7574–7579 (2015). doi: [10.1039/C5NR00889A](https://doi.org/10.1039/C5NR00889A); pmid: [25864409](https://pubmed.ncbi.nlm.nih.gov/25864409/)
117. J. A. Miwa *et al.*, van der Waals epitaxy of two-dimensional MoS₂-graphene heterostructures in ultrahigh vacuum. *ACS Nano* **9**, 6502–6510 (2015). doi: [10.1021/acsnano.5b02345](https://doi.org/10.1021/acsnano.5b02345); pmid: [26039108](https://pubmed.ncbi.nlm.nih.gov/26039108/)
118. Y. Shi *et al.*, van der Waals epitaxy of MoS₂ layers using graphene as growth templates. *Nano Lett.* **12**, 2784–2791 (2012). doi: [10.1021/nl204562j](https://doi.org/10.1021/nl204562j); pmid: [22642717](https://pubmed.ncbi.nlm.nih.gov/22642717/)
119. Y. C. Lin *et al.*, Direct synthesis of van der Waals solids. *ACS Nano* **8**, 3715–3723 (2014). doi: [10.1021/nr5003858](https://doi.org/10.1021/nr5003858); pmid: [24641706](https://pubmed.ncbi.nlm.nih.gov/24641706/)
120. L. Yu *et al.*, Graphene/MoS₂ hybrid technology for large-scale two-dimensional electronics. *Nano Lett.* **14**, 3055–3063 (2014). doi: [10.1021/nl404795z](https://doi.org/10.1021/nl404795z); pmid: [24810658](https://pubmed.ncbi.nlm.nih.gov/24810658/)
121. X. Li *et al.*, van der Waals epitaxial growth of two-dimensional single-crystalline GaSe domains on graphene. *ACS Nano* **9**, 8078–8088 (2015). doi: [10.1021/acsnano.5b01943](https://doi.org/10.1021/acsnano.5b01943); pmid: [26202730](https://pubmed.ncbi.nlm.nih.gov/26202730/)
122. A. Yan *et al.*, Direct growth of single- and few-layer MoS₂ on h-BN with preferred relative rotation angles. *Nano Lett.* **15**, 6324–6331 (2015). doi: [10.1021/acs.nanolett.5b01311](https://doi.org/10.1021/acs.nanolett.5b01311); pmid: [26317240](https://pubmed.ncbi.nlm.nih.gov/26317240/)
123. S. Wang, X. Wang, J. H. Warner, All chemical vapor deposition growth of MoS₂-h-BN vertical van der Waals heterostructures. *ACS Nano* **9**, 5246–5254 (2015). doi: [10.1021/acsnano.5b00655](https://doi.org/10.1021/acsnano.5b00655); pmid: [25895108](https://pubmed.ncbi.nlm.nih.gov/25895108/)
124. M. Cattelan *et al.*, New strategy for the growth of complex heterostructures based on different 2D materials. *Chem. Mater.* **27**, 4105–4113 (2015). doi: [10.1021/acs.chemmater.5b01170](https://doi.org/10.1021/acs.chemmater.5b01170)
125. H. C. Diaz, R. Chaghi, Y. J. Ma, M. Batzill, Molecular beam epitaxy of the van der Waals heterostructure MoTe₂ on MoS₂: Phase, thermal, and chemical stability. *2D Mater.* **2**, 044010 (2015). doi: [10.1088/2053-1583/2/4/044010](https://doi.org/10.1088/2053-1583/2/4/044010)
126. Y. Gong *et al.*, Vertical and in-plane heterostructures from WS₂/MoS₂ monolayers. *Nat. Mater.* **13**, 1135–1142 (2014). doi: [10.1038/nmat4091](https://doi.org/10.1038/nmat4091); pmid: [25262094](https://pubmed.ncbi.nlm.nih.gov/25262094/)
127. M. B. Alemayehu *et al.*, Designed synthesis of van der Waals heterostructures: The power of kinetic control. *Angew. Chem. Int. Ed.* **54**, 15468–15472 (2015). doi: [10.1002/anie.201506152](https://doi.org/10.1002/anie.201506152)
128. E. Xenogiannopoulou *et al.*, High-quality, large-area MoSe₂ and MoSe₂/Bi₂Se₃ heterostructures on AlN(0001)/Si(111) substrates by molecular beam epitaxy. *Nanoscale* **7**, 7896–7905 (2015). doi: [10.1039/C4NR06874B](https://doi.org/10.1039/C4NR06874B); pmid: [25856730](https://pubmed.ncbi.nlm.nih.gov/25856730/)
129. K. E. Aretouli *et al.*, Two-dimensional semiconductor HfSe₂ and MoSe₂/HfSe₂ van der Waals heterostructures by molecular beam epitaxy. *Appl. Phys. Lett.* **106**, 143105 (2015). doi: [10.1063/1.4917422](https://doi.org/10.1063/1.4917422)
130. A. Koma, K. Sunouchi, T. Miyajima, Fabrication of ultrathin heterostructures with van der Waals epitaxy. *J. Vac. Sci. Technol. B* **3**, 724 (1985). doi: [10.1116/1.583125](https://doi.org/10.1116/1.583125)
131. F. S. Ohuchi, B. A. Parkinson, K. Ueno, A. Koma, van der Waals epitaxial growth and characterization of MoSe₂ thin films on SnS₂. *J. Appl. Phys.* **68**, 2168–2175 (1990). doi: [10.1063/1.346574](https://doi.org/10.1063/1.346574)
132. K. Ueno, K. Saiki, T. Shimada, A. Koma, Epitaxial growth of transition metal dichalcogenides on cleaved faces of mica. *J. Vac. Sci. Technol. A* **8**, 68–72 (1990). doi: [10.1116/1.576983](https://doi.org/10.1116/1.576983)
133. Y. C. Lin *et al.*, Atomically thin heterostructures based on single-layer tungsten diselenide and graphene. *Nano Lett.* **14**, 6936–6941 (2014). doi: [10.1021/nl503144a](https://doi.org/10.1021/nl503144a); pmid: [25383798](https://pubmed.ncbi.nlm.nih.gov/25383798/)
134. X. Liu *et al.*, Rotationally commensurate growth of MoS₂ on epitaxial graphene. *ACS Nano* **10**, 1067–1075 (2016). doi: [10.1021/acsnano.5b06398](https://doi.org/10.1021/acsnano.5b06398); pmid: [26565112](https://pubmed.ncbi.nlm.nih.gov/26565112/)
135. A. Azizi *et al.*, Freestanding van der Waals heterostructures of graphene and transition metal dichalcogenides. *ACS Nano* **9**, 4882–4890 (2015). doi: [10.1021/acsnano.5b01677](https://doi.org/10.1021/acsnano.5b01677); pmid: [25885122](https://pubmed.ncbi.nlm.nih.gov/25885122/)
136. M. P. Levendorf *et al.*, Graphene and boron nitride lateral heterostructures for atomically thin circuitry. *Nature* **488**, 627–632 (2012). doi: [10.1038/nature11408](https://doi.org/10.1038/nature11408); pmid: [22932386](https://pubmed.ncbi.nlm.nih.gov/22932386/)
137. C. Huang *et al.*, Lateral heterojunctions within monolayer MoSe₂-WSe₂ semiconductors. *Nat. Mater.* **13**, 1096–1101 (2014). doi: [10.1038/nmat4064](https://doi.org/10.1038/nmat4064); pmid: [25150560](https://pubmed.ncbi.nlm.nih.gov/25150560/)
138. M. Y. Li *et al.*, Epitaxial growth of a monolayer WSe₂-MoS₂ lateral p-n junction with an atomically sharp interface. *Science* **349**, 524–528 (2015). doi: [10.1126/science.aab4097](https://doi.org/10.1126/science.aab4097); pmid: [26228146](https://pubmed.ncbi.nlm.nih.gov/26228146/)
139. X. Q. Zhang, C. H. Lin, Y. W. Tseng, K. H. Huang, Y. H. Lee, Synthesis of lateral heterostructures of semiconducting atomic layers. *Nano Lett.* **15**, 410–415 (2015). doi: [10.1021/nl503744f](https://doi.org/10.1021/nl503744f); pmid: [25494614](https://pubmed.ncbi.nlm.nih.gov/25494614/)

ACKNOWLEDGMENTS

This work was supported by the European Union FP7 Graphene Flagship Project 604391, European Research Council Synergy Grant, Hetero2D, Engineering and Physical Sciences Research Council (EPSRC) (Toward Engineering Grand Challenges), the Royal Society, U.S. Army Research Office, U.S. Navy Research Office, and U.S. Airforce Research Office. A.M. acknowledges support of EPSRC Early Career Fellowship EP/N007131/1. A.H.C.N. and A.C. acknowledge the National Research Foundation of Singapore under the Prime Minister's Office for Financial support under the Mid Size Centre Grant. We thank A. K. Geim, I. V. Grigorieva, V. I. Fal'ko, R. V. Gorbachev, F. Withers, A. V. Kretinin, C. Gesner, and S. J. Haigh.

10.1126/science.aac9439



2D materials and van der Waals heterostructures

K. S. Novoselov, A. Mishchenko, A. Carvalho and A. H. Castro

Neto (July 28, 2016)

Science **353** (6298), . [doi: 10.1126/science.aac9439]

EXTENDED PDF FORMAT
SPONSORED BY



www.rndsystems.com

Editor's Summary

This copy is for your personal, non-commercial use only.

- | | |
|----------------------|--------------------------------------------------------------------------------------------------------------------------------------------------------------------------------------------------------------------------|
| Article Tools | Visit the online version of this article to access the personalization and article tools:
http://science.sciencemag.org/content/353/6298/aac9439 |
| Permissions | Obtain information about reproducing this article:
http://www.sciencemag.org/about/permissions.dtl |

Science (print ISSN 0036-8075; online ISSN 1095-9203) is published weekly, except the last week in December, by the American Association for the Advancement of Science, 1200 New York Avenue NW, Washington, DC 20005. Copyright 2016 by the American Association for the Advancement of Science; all rights reserved. The title *Science* is a registered trademark of AAAS.